



OPEN

# Spatial patterns of tumour growth impact clonal diversification in a computational model and the TRACERx Renal study

Xiao Fu<sup>1,2,24</sup>, Yue Zhao<sup>3,4,5,6,24</sup>, Jose I. Lopez<sup>7</sup>, Andrew Rowan<sup>3</sup>, Lewis Au<sup>8,9</sup>, Annika Fendler<sup>10</sup>, Steve Hazell<sup>10</sup>, Hang Xu<sup>3,11</sup>, Stuart Horswell<sup>12</sup>, Scott T. C. Shepherd<sup>10,8,9</sup>, Charlotte E. Spencer<sup>8,9</sup>, Lavinia Spain<sup>8,9</sup>, Fiona Byrne<sup>10</sup>, Gordon Stamp<sup>13</sup>, Tim O'Brien<sup>14</sup>, David Nicol<sup>15</sup>, Marcellus Augustine<sup>3</sup>, Ashish Chandra<sup>16</sup>, Sarah Rudman<sup>17</sup>, Antonia Toncheva<sup>18</sup>, Andrew J. S. Furness<sup>8,9</sup>, Lisa Pickering<sup>10</sup>, Santosh Kumar<sup>19</sup>, Dow-Mu Koh<sup>19,20</sup>, Christina Messiou<sup>19,20</sup>, Derfel ap Dafydd<sup>20</sup>, Matthew R. Orton<sup>21</sup>, Simon J. Doran<sup>19</sup>, James Larkin<sup>9</sup>, Charles Swanton<sup>3,4,22</sup>, Erik Sahai<sup>2</sup> ✉, Kevin Litchfield<sup>3,4,23</sup> ✉, Samra Turajlic<sup>8,9</sup> ✉, on behalf of the TRACERx Renal Consortium and Paul A. Bates<sup>1</sup> ✉

**Genetic intra-tumour heterogeneity fuels clonal evolution, but our understanding of clinically relevant clonal dynamics remain limited. We investigated spatial and temporal features of clonal diversification in clear cell renal cell carcinoma through a combination of modelling and real tumour analysis. We observe that the mode of tumour growth, surface or volume, impacts the extent of subclonal diversification, enabling interpretation of clonal diversity in patient tumours. Specific patterns of proliferation and necrosis explain clonal expansion and emergence of parallel evolution and microdiversity in tumours. In silico time-course studies reveal the appearance of budding structures before detectable subclonal diversification. Intriguingly, we observe radiological evidence of budding structures in early-stage clear cell renal cell carcinoma, indicating that future clonal evolution may be predictable from imaging. Our findings offer a window into the temporal and spatial features of clinically relevant clonal evolution.**

The development of cancer is an evolutionary process<sup>1,2</sup>. Acquisition of genomic alterations including mutations and somatic copy-number alterations (SCNAs) drives the emergence of genetically heterogeneous subpopulations of cancer cells or subclones<sup>3</sup>, resulting in intra-tumour heterogeneity (ITH). A subset of genomic alterations (termed 'drivers') endows subclones with increased fitness. Subclones compete for resources, including physical space, and undergo expansion or extinction according to their fitness under selective pressures imposed by the tumour micro-environment (TME) or therapeutic intervention. With advances in next-generation sequencing, clonal architecture and evolutionary features have been elucidated in a variety of tumour types<sup>4-7</sup>. However, the ability to predict clinically relevant evolutionary trajectories remains limited.

One potential to enhance this ability lies in the detection and characterization of ongoing clonal evolution. ITH provides a substrate for the selection of competent clones<sup>8</sup>. Detection of ITH is sampling dependent, and accurate measurement of diversity is enhanced by sampling of multiple small tumour areas<sup>9</sup>. While macrodiversity (that is, the number of subclones in the whole tumour) reflects the established clonal diversity within a tumour, clonal diversity at a narrow spatial scale, or microdiversity (that is, the number of subclones within a single tumour sample), could represent under-detected ongoing clonal evolution (Fig. 1a). Both macrodiversity<sup>6,7</sup> and microdiversity have clinical implications. Microdiversity predicts poor survival in paediatric kidney cancer<sup>10</sup> and contributes to invasion in breast tumours<sup>11</sup>. Clonal diversification sometimes manifests as parallel evolution, that is, the selection

<sup>1</sup>Biomolecular Modelling Laboratory, The Francis Crick Institute, London, UK. <sup>2</sup>Tumour Cell Biology Laboratory, The Francis Crick Institute, London, UK. <sup>3</sup>Cancer Evolution and Genome Instability Laboratory, The Francis Crick Institute, London, UK. <sup>4</sup>Cancer Research UK Lung Cancer Centre of Excellence, University College London Cancer Institute, London, UK. <sup>5</sup>Department of Thoracic Surgery, Fudan University Shanghai Cancer Center, Shanghai, China. <sup>6</sup>Department of Oncology, Shanghai Medical College, Fudan University, Shanghai, China. <sup>7</sup>Department of Pathology, Cruces University Hospital, Biocruces-Bizkaia Institute, Barakaldo, Spain. <sup>8</sup>Cancer Dynamics Laboratory, The Francis Crick Institute, London, UK. <sup>9</sup>Renal and Skin Units, The Royal Marsden Hospital, London, UK. <sup>10</sup>Department of Pathology, the Royal Marsden NHS Foundation Trust, London, UK. <sup>11</sup>Stanford Cancer Institute, Stanford University School of Medicine, Stanford, CA, USA. <sup>12</sup>Department of Bioinformatics and Biostatistics, The Francis Crick Institute, London, UK. <sup>13</sup>Experimental Histopathology Laboratory, The Francis Crick Institute, London, UK. <sup>14</sup>Urology Centre, Guy's and St. Thomas' NHS Foundation Trust, London, UK. <sup>15</sup>Department of Urology, the Royal Marsden NHS Foundation Trust, London, UK. <sup>16</sup>Department of Pathology, Guy's and St. Thomas' NHS Foundation Trust, London, UK. <sup>17</sup>Department of Medical Oncology, Guy's and St. Thomas' NHS Foundation Trust, London, UK. <sup>18</sup>Biobank, Guy's and St. Thomas' NHS Foundation Trust, London, UK. <sup>19</sup>Division of Radiotherapy and Imaging, Institute of Cancer Research, Sutton, UK. <sup>20</sup>Department of Radiology, Royal Marsden Hospital, London, UK. <sup>21</sup>Artificial Intelligence Imaging Hub, Royal Marsden NHS Foundation Trust, Sutton, UK. <sup>22</sup>Department of Medical Oncology, University College London Hospitals, London, UK. <sup>23</sup>Tumour Immunogenomics and Immunosurveillance Laboratory, University College London Cancer Institute, London, UK. <sup>24</sup>These authors contributed equally: Xiao Fu, Yue Zhao. \*A list of authors and their affiliations appears at the end of the paper. ✉e-mail: [erik.sahai@crick.ac.uk](mailto:erik.sahai@crick.ac.uk); [k.litchfield@ucl.ac.uk](mailto:k.litchfield@ucl.ac.uk); [samra.turajlic@crick.ac.uk](mailto:samra.turajlic@crick.ac.uk); [paul.bates@crick.ac.uk](mailto:paul.bates@crick.ac.uk)

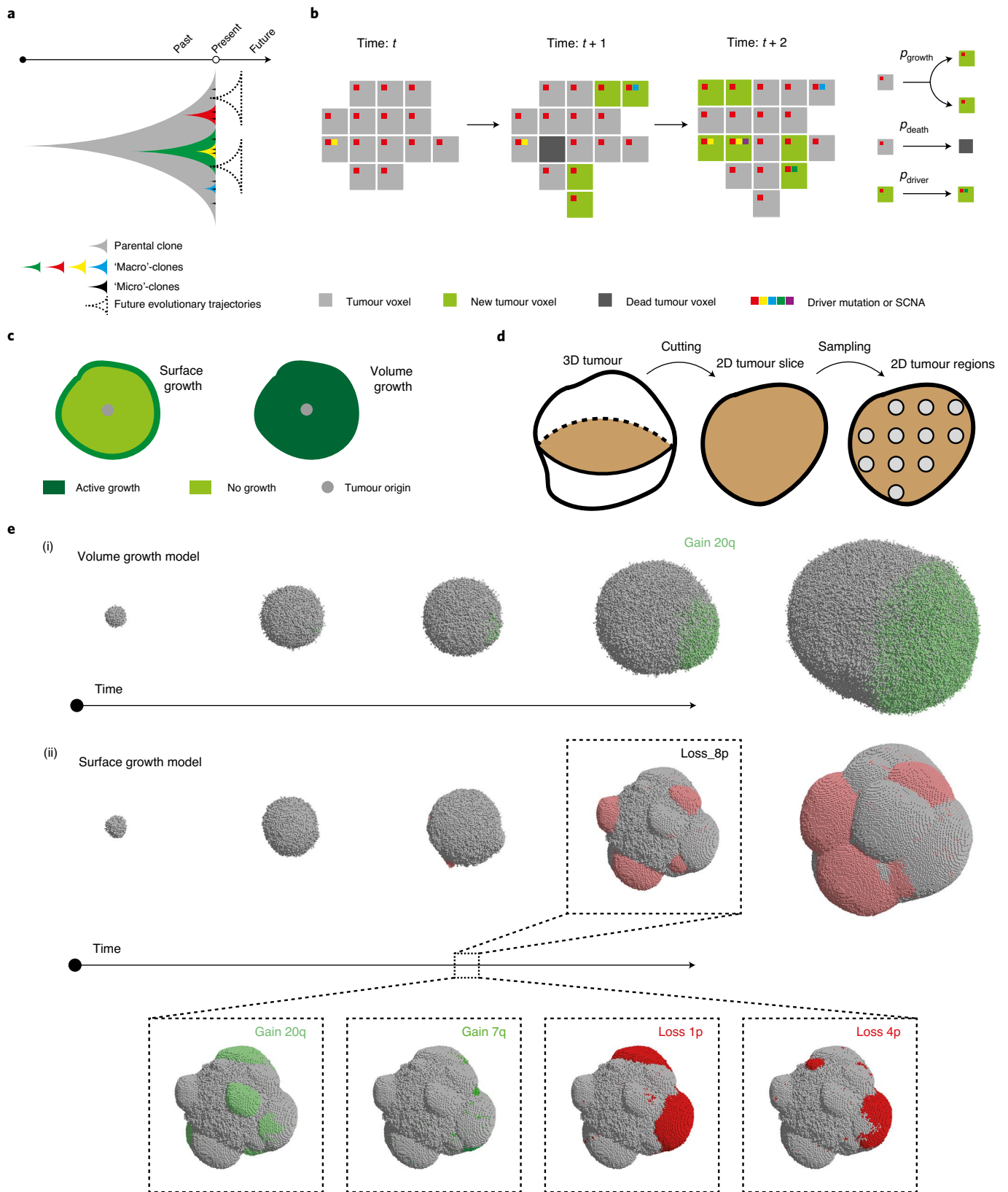


**Fig. 1 | Construction of in silico tumours.** **a**, Schematic illustrating future evolutionary trajectories delineated by present under-detected subclones. **b**, Schematic of probabilistic growth, death and driver acquisition in a coarse-grained cellular automaton model. **c**, Schematic of two growth modes: 'surface growth' with proliferation predominating at the tumour surface and 'volume growth' with proliferation throughout the tumour volume. **d**, Schematic figure of three levels of measurements: from 3D tumour to 2D tumour slice and 2D tumour regions within the slice. **e**, Representative in silico tumours under volume growth (i) and surface growth (ii), respectively, from a 3D view, showing tumour voxels harbouring gain of chromosome arm events (green) and loss of chromosome arm events (red), with different shades reflecting different driver events.

of distinct mutations in the same gene in distinct subclones<sup>4,5,7,12–15</sup>. More recently, parallel evolution of SCNAs was demonstrated through mirrored subclonal allelic imbalance<sup>16</sup>. Thus, understanding microdiversity could offer important insights into clinically relevant evolutionary potential.

Despite increasing understanding of ITH and macrodiversity, understanding of the temporal features of clonal evolution remains limited owing to ethical and logistical challenges in obtaining serial single- or multi-regional biopsies from patients<sup>17</sup>. While longitudinal profiling of circulating tumour DNA permits clonal tracking over time<sup>18–21</sup>, this approach provides no resolution of the spatial outgrowth or organization of clones. To improve the understanding of spatial and temporal features of clonal diversification, we developed a coarse-grained cellular automata model of tumour growth with stochastic acquisition of driver events (Fig. 1b). Various forms of non-spatial mathematical models have been formulated to describe different types of tumour growth dynamics, including exponential and polynomial growth<sup>22,23</sup>. More recently, modelling work incorporating spatial elements of tumour growth found an impact of growth modes on the classification of neutral evolution and selection<sup>24–27</sup>. Previous analysis of clear cell renal cell carcinoma (ccRCC) supports the predominance of active proliferation at the tumour surface in a subset of tumours<sup>28</sup>, and we recently described varying rates of proliferation across the tumour<sup>29</sup>. In this study, we evaluated the effects of different tumour growth modes on spatial and temporal features of clonal diversification in our model, focusing on two simple growth modes: (i) uniform growth throughout the tumour volume (referred to as the ‘volume growth model’) and (ii) active proliferation restricted to the tumour surface (referred to as the ‘surface growth model’) (Methods and Fig. 1c). We additionally investigated a broader set of model conditions including the implementation of necrosis in the tumour interior, building upon our recent study<sup>29</sup>. We related our model to the TRACERx Cancer Evolution through therapy (Rx) (TRACERx) Renal study, which previously evaluated the genomic profiles and spatial coordinates of 756 patient tumour (PT) regions from 66 tumours<sup>29</sup>. Tumours with high clonal diversity do not necessarily harbour metastasizing clones<sup>30</sup>, suggesting that the development of metastatic competence and continuing subclonal diversification may be uncoupled in the tumour as independent evolutionary processes. Through combined modelling and clinical analysis, we show how tumour growth modes determine the extent and trajectories of clonal diversity. Crucially, we explore temporal aspects of tumour evolution that would otherwise be inaccessible from single-timepoint biopsies.

## Results

### Generation of an agent-based model recapitulating ccRCC evolution.

To understand the spatial and temporal features of clonal

diversification, we developed a coarse-grained cellular automaton model to simulate the evolutionary dynamics of ccRCCs (see Methods for a detailed description). The model includes 12 genes and 14 SCNAs (Extended Data Fig. 1) identified as canonical driver events in ccRCCs in the TRACERx Renal study<sup>7</sup>. Each model unit, referred to as a ‘tumour voxel’, represents a tumour volume of 1 mm<sup>3</sup>. Tumour voxels stochastically undergo growth, death and acquisition of driver events upon growth. As proliferation proceeds, some tumour voxel acquires a driver event conferring selective advantages, manifested in the current study as an increase in the growth probability ( $p_{\text{growth}}$ ). Two ways of implementing selective advantages are considered, being referred to as ‘saturated’ and ‘additive’ driver advantage models. In the saturated driver advantage model, the  $p_{\text{growth}}$  of a tumour voxel can be at one of three levels  $\{p_{\text{growth}}^{(\text{initial})}, p_{\text{growth}}^{(\text{moderate})}, p_{\text{growth}}^{(\text{maximal})}\}$ . Each driver endows a tumour voxel with one of these levels, and the relative differences in selective advantage of drivers, denoted as  $s$ , are assumed to reflect their association with the Ki67 score in tumour regions (Extended Data Fig. 1) and their frequencies in the clinical cohort<sup>7</sup>. For simplicity, individual driver gene mutations are assigned with  $p_{\text{growth}}^{(\text{initial})}$ , whereas four SCNAs with strong association with Ki67 score (7q gain, 20q gain, 4q loss and 8p loss) are assumed to be the strongest drivers assigned with  $p_{\text{growth}}^{(\text{maximal})}$ , and therefore their acquisition would lead to the biggest increase in growth probability. Importantly, the saturated model is implemented with only two levels of selective advantage, and the growth probability of a tumour voxel becomes saturated at 1 if acquiring the strongest driver. The additive driver advantage model has a more graduated implementation of selective advantage in which the growth probability of a tumour voxel is defined by all the drivers it harbours,

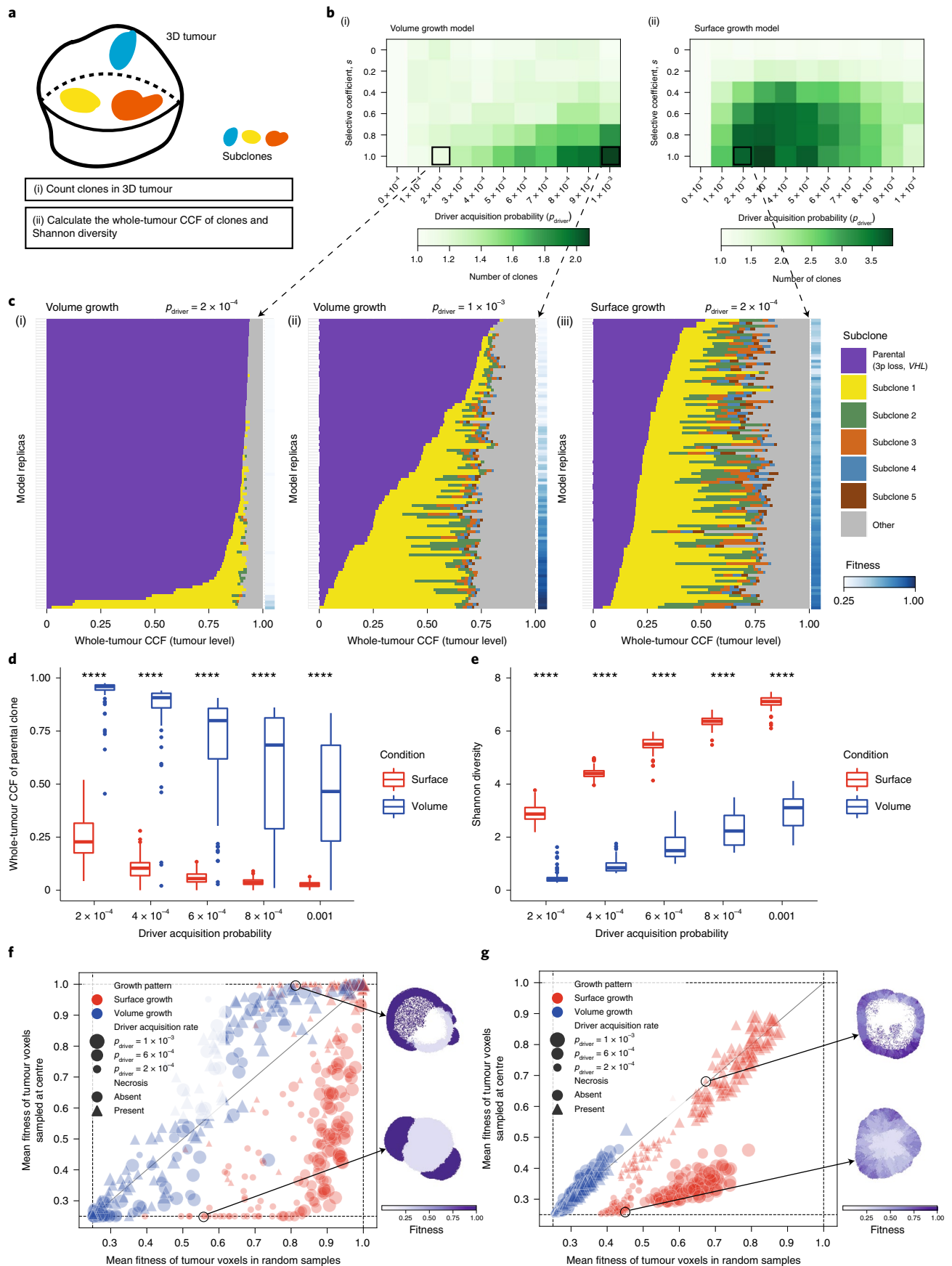
$p_{\text{growth}} = p_{\text{growth}}^{(\text{initial})} + \sum_k p_{\text{growth}_k}$ , where  $p_{\text{growth}_k}$  reflects the amount of growth probability added by driver  $k$  (Extended Data Fig. 2). The amount  $p_{\text{growth}_k}$  varies between drivers and is assigned according to different strengths of their association with Ki67 score (Extended Data Figs. 1 and 2).

Additional assumptions are made to keep the model minimal. Individual driver gene mutations are assumed to be acquired with a greater probability ( $p_{\text{driver}}$ ) than SCNAs. A second mutation in the same gene is assumed to never occur in the same tumour voxel. As the majority of ccRCCs have clonal *VHL* inactivation events, in general and in the TRACERx Renal cohort<sup>7</sup>, the founder tumour voxel is assumed to harbour *VHL* inactivation together with 3p loss as a clonal event. Based on data from the TRACERx Renal study<sup>7</sup>, and functional evidence<sup>31,32</sup>, mutations in *PBRM1* or *BAP1* are assumed to enhance the probability of SCNA acquisition.

**Fig. 2 | Growth modes impact the extent of clonal diversification and tumour fitness.** **a**, Schematic of the whole-tumour analysis of clonal diversity. **b**, Heatmap showing the average number of clones (that is, parental clone and subclones) with respect to driver acquisition probability ( $p_{\text{driver}}$ ) and selective coefficient ( $s$ ) in the volume growth (i) and surface growth (ii) models. The average is calculated from 50 in silico tumours per parameter condition. Clones with a whole-tumour CCF of at least 0.05 are counted. **c**, Whole-tumour CCF of parental and largest subclones in in silico tumours under volume growth (i,ii) and surface growth (iii), respectively. Average fitness in a tumour slice for each simulation is presented as a heatmap. Driver acquisition probabilities in these sets of simulations are  $p_{\text{driver}} = 2 \times 10^{-4}$  (i),  $1 \times 10^{-3}$  (ii) and  $2 \times 10^{-4}$  (iii). ‘Parental (3p loss, *VHL*)’ clone is shown along with up to five subclones with a whole-tumour CCF of 0.01 or higher. All remaining subclones are represented in the ‘other’ group. **d**, Whole-tumour CCF of parental clone in in silico tumours under volume growth and surface growth with varying driver acquisition probabilities.  $n = 100$  for each condition. **e**, Shannon diversity index in in silico tumours under volume growth and surface growth with varying driver acquisition probabilities.  $n = 100$  for each condition. **f,g**, Mean fitness of randomly sampled (10% of all) tumour voxels against the mean fitness of the central-most (10%) tumour voxels, in models with saturated (**f**) and additive (**g**) driver advantages. Data points reflect sets of simulations with varying growth patterns (colour), driver acquisition rates (size) and implementation of necrosis (symbol). Heatmaps indicate the fitness in representative in silico tumours under surface growth without or with the implementation of necrosis. Statistical annotations in **d** and **e** reflect two-sided Wilcoxon tests: \*\*\*\*  $P \leq 0.0001$ . In box plots in **d** and **e**, the ends of the box reflect the lower (Q1) and upper (Q3) quartiles, with the difference indicating the IQR; the horizontal line dividing the box reflects the median; the ends of the vertical line indicate the extreme values within the range from  $Q1 - 1.5 \times \text{IQR}$  to  $Q3 + 1.5 \times \text{IQR}$ ; dots beyond the vertical line indicate potential outliers.

Mutations and acquisition of SCNAs are assumed to be proliferation dependent, which implies that DNA replication and chromosome mis-segregation are the main source of genomic alterations. Lastly,

the selective advantage endowed by a driver is assumed to be fixed, so the variation in driver advantage dependent on changing environments is not considered in the current study.





Each simulation starts from a single tumour voxel carrying *VHL* and 3p loss and ends when the size exceeds 1 million tumour voxels, reflecting a tumour diameter of approximately 12 cm. Simulated tumours are analysed at multiple spatial scales (Fig. 1d). A flow diagram of the simulation procedure is presented in Extended Data Fig. 3.

**Growth modes impact the extent of clonal diversification.** We hypothesized that the growth mode influences the extent of clonal diversification. To test this, we first assessed the clonal diversity at the end of a simulation. Tumours under volume growth commonly harboured only parental clone with the lack of further subclonal diversification or contained a single dominant subclone, whereas tumours under surface growth harboured multiple advantageous subclones (Fig. 1e). Intriguingly, expanding subclones in tumours under surface growth were also associated with changes in tumour morphology. These subclones initially appeared as bulging structures in a localized manner and subsequently outgrew to cover large areas of the tumour surface. Next, we counted the number of clones in the whole tumour (Fig. 2a,b). Under volume growth, subclones were only observed in tumours with larger  $s$  and larger  $p_{\text{driver}}$  (Fig. 2b). By contrast, under the surface growth model, for a wide range of  $s$ , tumours with small to moderate  $p_{\text{driver}}$  harboured more subclones (Fig. 2b). We then illustrated the fractions of a tumour that subpopulations occupied and tumour fitness (measured as the average growth probabilities of tumour voxels in a tumour slice, Methods). Overall, volume growth models depicted a dichotomous pattern of clonal evolution and fitness: limited evidence of clonal diversification with low tumour fitness (Fig. 2c(i)) or presence of a single dominant clone with high tumour fitness (Fig. 2c(ii)). The latter pattern reflected early fixation of a highly fit clone in a subset of ‘born to be bad’ tumours. In comparison, in the surface growth model, extensive subclonal diversification and enhanced tumour fitness were evident in nearly all cases, even with a small  $p_{\text{driver}}$  (Fig. 2c(iii)). With a large  $p_{\text{driver}}$ , almost all tumours achieved peak fitness (Extended Data Fig. 1). More extensive subclonal diversification was also noted in models with additive driver advantages (Supplementary Note 1 and Extended Data Fig. 2). These differences between growth models were quantitatively reflected in the whole-tumour cancer cell fraction (CCF) of the parental clone (Fig. 2d) and Shannon diversity index (Methods and Fig. 2e). Using these two metrics, greater extent of diversification in the surface growth model was also noted for conditions with still smaller  $p_{\text{driver}}$  (Supplementary Fig. 1) or smaller  $s$  (Supplementary Fig. 2). In the interest of characterizing patterns of subclonal diversification and contrasting the two growth modes, we limit our parameter analysis, to  $s = 1$  and a range of  $p_{\text{driver}}$  from  $2 \times 10^{-4}$  to  $1 \times 10^{-3}$ .

We further incorporated central necrosis into a subset of models to evaluate its impact on clonal diversification<sup>29</sup>. In brief, where necrosis was incorporated, tumour voxels located far from

the tumour surface underwent death with an elevated probability ( $p_{\text{necrosis}} = 0.5$ ) (Methods). In both growth modes, incorporation of necrosis generally led to a greater extent of clonal evolution and higher fitness observed at the end of simulations (Extended Data Fig. 4 and Supplementary Fig. 3). To further investigate the impact of necrosis on fitness at different parts of a tumour, we collected samples of centrally, marginally or randomly located tumour voxels (Methods). Surface growth models in general achieved higher fitness than volume growth models, as evidenced in random samples (Fig. 2f,g and Supplementary Figs. 4 and 5). When necrosis was implemented, fitness in the tumour centre was significantly elevated in the surface growth models (Fig. 2f,g, Supplementary Note 2 and Supplementary Figs. 4 and 5), in keeping with our recent study<sup>29</sup>. More broadly, surface growth led to more extensive subclonal diversification, corresponding to highly branched tumour evolution, while volume growth resulted either in tumours with limited evidence of clonal diversification or in tumours with early fixation of a fit subclone corresponding to punctuated evolution. Interestingly, these modes of evolution correspond to evolutionary subtypes identified in ccRCC<sup>7</sup>. A subset of tumours with low fitness has limited subclonal diversification, while other tumours have an early fixation of a highly fit clone resulting in rapid clonal sweep<sup>7</sup>. There are also tumours with extensive subclonal diversification, characterized by a range of drivers.

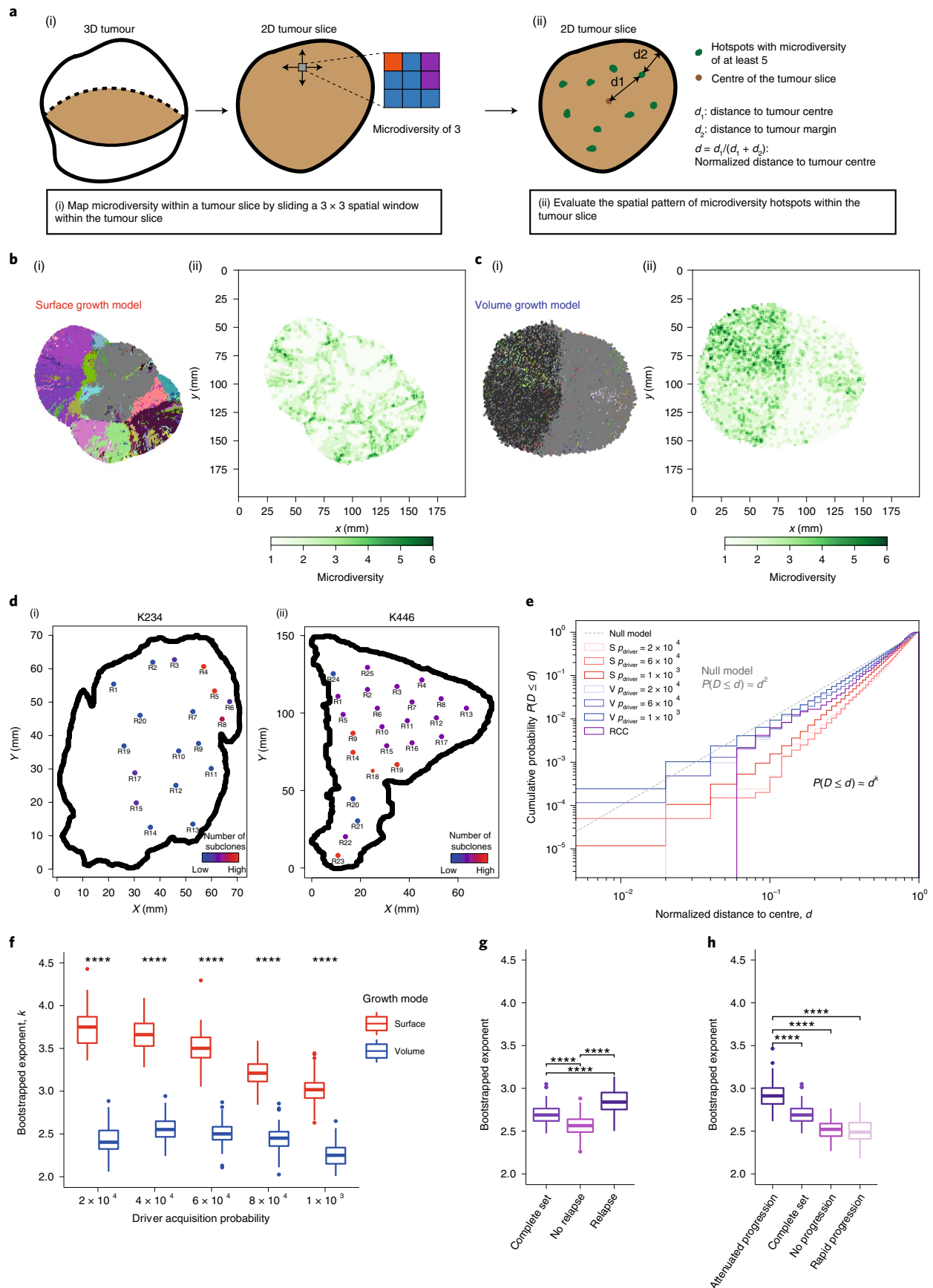
**Growth modes impact the spatial distribution of clonal diversity.** We next examined the spatial distribution of clonal diversity (Fig. 3a and Methods). Under surface growth, multiple subclones, representing macrodiversity, outgrew to occupy distinct spatially contiguous areas with hotspots of microdiversity frequent near the tumour edge (Fig. 3b). In the representative volume growth model, a single dominant subclone was observed with a more uniform distribution of microdiversity hotspots (Fig. 3c). Next, we explored whether similar patterns were present in ccRCC. Using regions that contain at least two subclones as a proxy for microdiversity hotspots in the TRACERx Renal data, we observed both spatial patterns of microdiversity corresponding to the surface growth model (for example, ‘K234’) and volume growth model (for example, ‘K446’) (Fig. 3d). Consistently between the surface growth model and clinical data, while microdiversity was generally high near the edge, there was variation along the edge, with higher microdiversity apparently at the more bulging regions.

Intriguingly, the cumulative probability distribution with respect to the normalized distance from microdiversity hotspots to tumour centre,  $d$ , depicted power-law scaling (Fig. 3e), suggesting that the probability of observing spots with high microdiversity along the radius of a tumour could be estimated using a simple mathematical formula (that is,  $P(D \leq d) \approx d^k$ , where  $k$  is the power-law exponent to be fitted). In comparison, the surface growth model displayed a larger  $k$  (Fig. 3f and Supplementary Fig. 6), indicating a greater

**Fig. 3 | Growth modes impact the spatial features of clonal diversification.** **a**, Schematic figure and procedure for the analysis of microdiversity within a 2D tumour slice. **b,c**, Spatial maps of subclones (i) and microdiversity (ii) in a representative in silico tumour under surface growth (**b**) or volume growth (**c**) with  $p_{\text{driver}} = 2 \times 10^{-4}$ , showing tumour voxels that belong to the parental clone (grey) and other subclones (randomly generated colours). **d**, Maps of regional biopsies with the number of subclones within a biopsy, colour coded in two cases (K234 and K446) in the TRACERx Renal study. Hues from red to purple to blue reflect decreasing number of subclones. ‘Low’ and ‘High’ reflect one and four subclones in K234 or two and four subclones in K446, respectively. **e**, Cumulative probability distribution,  $P(D \leq d)$ , of the normalized distances to tumour centre in in silico tumours under surface growth and volume growth and in ccRCC tumours.  $n = 100$  for each model condition for surface growth (‘S’) and volume growth (‘V’).  $p_{\text{driver}} = 2 \times 10^{-4}$  indicates a driver acquisition probability of  $2 \times 10^{-4}$ . A total of 606 PT regions from 54 ccRCC tumours are considered for this analysis. ‘Null model’ reflects a power law with an exponent of 2. **f**, Bootstrapped power-law exponent  $k$ , as in  $P(D \leq d) \approx d^k$ , fitted to cumulative probability distributions generated from bootstrap samples (Methods) with  $n = 100$   $k$  values per condition. **g,h**, Bootstrapped power-law exponent  $k$  in ccRCC tumours partitioned according to relapse status (**g**) or rate of disease progression (**h**) with  $n = 100$   $k$  values per condition. Statistical annotations in **f–h** reflect two-sided Wilcoxon tests: \*\*\*\*  $P \leq 0.0001$ . In box plots in **f–h**, the ends of the box reflect the lower (Q1) and upper (Q3) quartiles, with the difference indicating the IQR; the horizontal line dividing the box reflects the median; the ends of the vertical line indicate the extreme values within the range from  $Q1 - 1.5 \times \text{IQR}$  to  $Q3 + 1.5 \times \text{IQR}$ ; dots beyond the vertical line indicate potential outliers.

likelihood of microdiversity hotspots being enriched near the tumour edge. Critically, spatial homogenization of subclone patterns abolished the characteristic scaling behaviour (Supplementary

Note 3 and Extended Data Fig. 5), demonstrating the importance of spatial elements of tumour growth in generating microdiversity. Models with additive driver advantages showed similar



distributions of microdiversity hotspots (Supplementary Note 4 and Extended Data Fig. 6). The incorporation of necrosis into the model re-adjusted the spatial profile in surface growth models, leading to the enrichment of additional microdiversity hotspots in the necrotic tumour centre (Supplementary Note 4 and Extended Data Fig. 6). The power-law pattern was also observed in 54 tumours with microdiversity hotspots (Fig. 3e). Moreover, there was an association between the power-law scaling exponent  $k$  with relapse status (Fig. 3g) and the rate of disease progression (Fig. 3h) in the TRACERx Renal study (Supplementary Table 1), where tumours mapped to a poorer clinical outcome are typically associated with a steeper spatial distribution of microdiversity hotspots and enrichment towards the tumour margin (Supplementary Note 5 and Supplementary Fig. 7). Tumours with attenuated progression showed a steep gradient of microdiversity hotspots, consistent with surface growth models. Interestingly, both tumours with no progression and those with rapid progression show a shallow gradient of microdiversity hotspots, nicely corresponding to volume growth models with limited evidence of evolution and with early fixation of a fit clone, respectively. The observation of spatial features of clonal diversity (Supplementary Table 2) adds to our previous finding that the overall genetic diversity correlated with patient clinical outcome<sup>7</sup>.

**Growth modes impact the spatial patterns of parallel evolution events and youngest subclones.** As subclonal diversification could involve acquisition of, and be facilitated by, distinct mutations in the same gene at spatially separate locations, we next evaluated the frequency of parallel evolution events and their spatial features. In the TRACERx Renal study, parallel evolution was observed in 28 tumours, with each event spanning a variable number of regions (Supplementary Note 6 and Supplementary Table 3). Interestingly, parallel mutation events with limited clonal expansion (spanning only a single region) showed distinct spatial patterns in different ccRCCs, suggesting that ongoing convergent evolution in the same gene could operate at varying locations of a tumour (Fig. 4a). In some cases (for example, K252), such events were all close to the margin; in other cases (for example, K520), they were located far from the edge (Fig. 4a,b). We hypothesized that the observed distinct patterns of parallel mutation events could be attributed to the patterns of proliferation and accordingly recent subclone births. To test this, we returned to the computational model and examined whether and how different growth models differ in the patterns of youngest subclones (Fig. 4c). Consistent with the patterns of microdiversity, we observed a preferential distribution of the youngest subclones near the tumour edge in the surface growth model and a more uniform distribution in the volume growth models (Fig. 4d(i) and Extended Data Fig. 7). Interestingly, when necrosis was incorporated, surface growth models often showed a bimodal distribution, with youngest subclones being born either near the tumour

surface or in the necrotic interior, a pattern that was rarely observed in volume growth models (Fig. 4d(ii)).

Motivated by the diverse patterns of youngest subclones observed in models with different growth modes, we then turned to the clinical data. Focusing on the 20 ccRCC cases most extensively sampled ( $n \geq 10$  regions) from TRACERx Renal, we observe events that spanned a single region (assumed to be the most recent/youngest subclones) close to the tumour margin (for example, K523, K360 and K234) and located at varying distances from the tumour margin (for example, K156, K165 and K272) (Fig. 4e,f and Extended Data Fig. 7). Observations of these representative cases characterized by high levels of clonal diversity<sup>7</sup> suggest that they evolved via surface growth but that necrosis in K156, K165 and K272 enabled birth of young subclones in the interior. Intriguingly, histological assessment of K156 showed the presence of paucicellular areas both macroscopically (Supplementary Fig. 8) and microscopically (Fig. 4g) in the interior of the tumour, which interfaced youngest subclones, in contrast to the interior of K523 (Fig. 4h). These observations suggest that continuing proliferation and clonal evolution occur at the tumour margin but are also facilitated by available space in the interior.

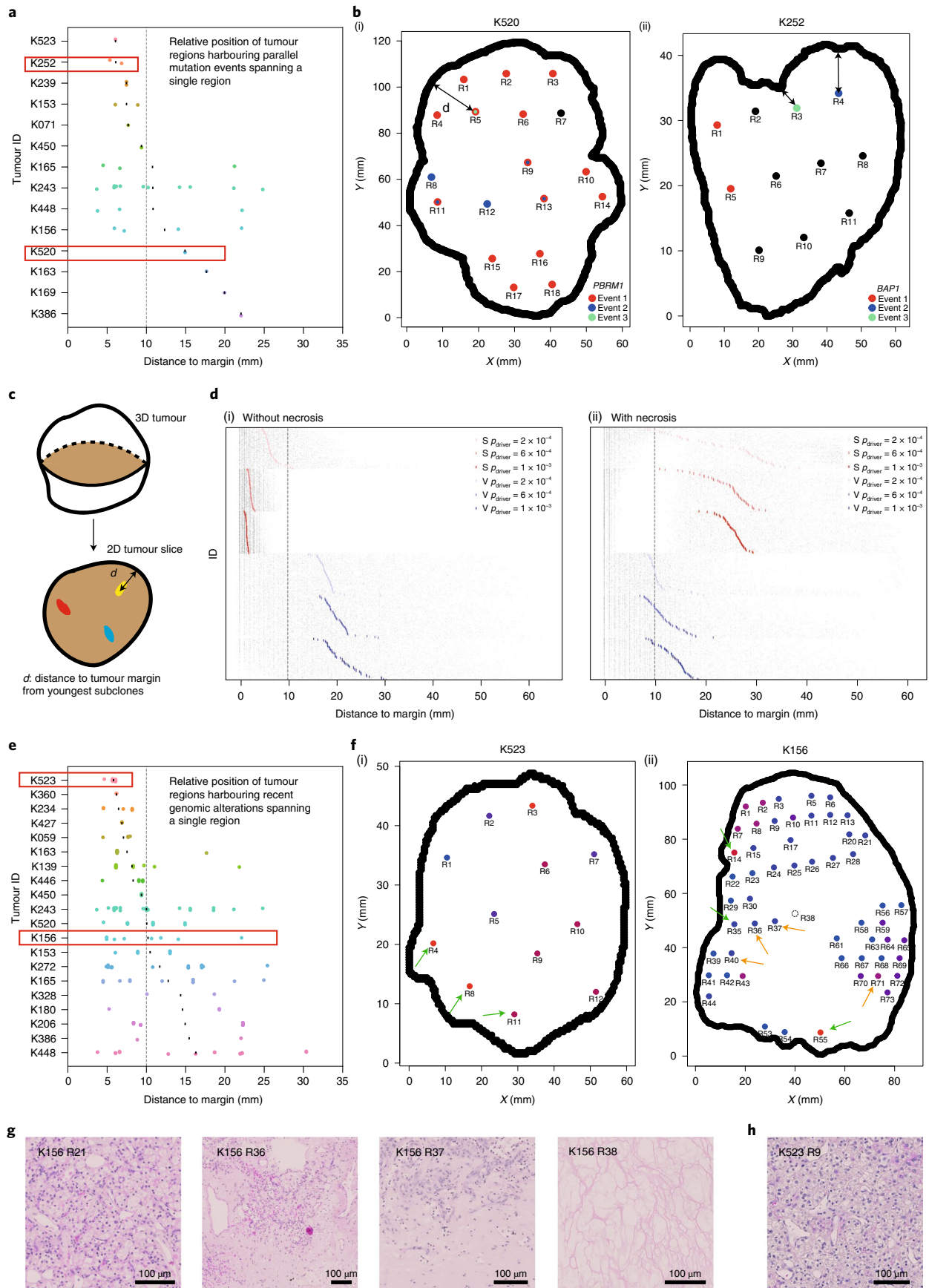
**Growth modes impact the temporal features of clonal diversification.** We investigated temporal features of clonal diversification through in silico time-course analysis. Overall, the number of subclones remained limited in volume growth models but increased over time before reaching a plateau in surface growth models (Fig. 5a,b and Extended Data Fig. 8). Thus, surface growth and volume growth models initially showed similar extent of clonal diversification with subsequent divergence. Notably, when necrosis was implemented, volume growth models were minimally impacted, but we observe a dramatic reduction in clonal diversity at later stages of tumour growth in surface growth models, especially when additive driver advantages were implemented (Extended Data Fig. 8). This reflected a 'pruning' effect on the clonal structure with elimination of the less fit subclones. These observations reconciled previous observation of a non-monotonic relationship between tumour size and number of clones, including the collapse of clonal diversity at very large tumour sizes<sup>7</sup>.

As the birth of a new subclone is defined by the acquisition of new driver events in a tumour voxel, expectedly, surface growth models, which showed more extensive clonal diversification, accumulated a larger number of drivers, at a faster rate, than volume growth models (Extended Data Fig. 8). Nevertheless, in contrast to the rate of clonal diversification, the number of accumulated drivers increased monotonically over time in the surface growth models. Repeat simulations under surface growth clearly exhibited an altered direction of 'evolutionary flows', indicating out-competence of advantageous subclones and reduction of overall clonal diversity at later stages (Fig. 5c). Underlying these observations, surface growth led to

**Fig. 4 | Growth modes impact the spatial features of parallel evolution and youngest subclones.** **a**, Distance from regions harbouring parallel mutational events that span a single region to the tumour margin. Red rectangles indicate the two representative cases shown in **b**. **b**, Maps of regions containing parallel mutation events in two representative cases (*PBRM1* events in K520 (i) and *BAP1* events in K252 (ii)) in the TRACERx Renal study. Distinct parallel mutation events are indicated using different colours. For regions containing more than two parallel mutations, two colours are applied simultaneously. Double-headed arrow indicates the measurement of distance to tumour edge. **c**, Schematic of the analysis of youngest subclones within a 2D tumour slice. **d**, Distance from the positions of youngest subclones to the tumour margin, in models without (i) or with (ii) the implementation of necrosis.  $n = 100$  youngest subclones from each simulation are analysed and shown as grey points, with the mean distance to margin indicated with a coloured vertical bar.  $n = 50$  simulations are shown, arranged from small to large mean distance to margin (top to bottom) for each model condition. Surface growth and volume growth models are shown in red and blue, respectively, with increasing driver acquisition probabilities indicated by increasing colour intensity. **e**, Distance from regions harbouring genomic alterations that span a single region to the tumour margin. Only tumours with at least ten regions are included. Red rectangles indicate the two representative cases shown in **f**. **f**, Maps of regional biopsies with the number of subclones within a biopsy colour coded in two representative cases (K523 and K156) in the TRACERx Renal study. Hues from red to purple to blue reflect decreasing number of subclones. 'Low' and 'High' reflect one and four subclones in K523 or one and six subclones in K156, respectively. Regions harbouring events that span a single region are marked by arrows, green if located within 10 mm from the tumour edge and orange otherwise. **g,h**, Histological images of representative areas from tumour regions of K156 (**g**) and K523 (**h**). Vertical dashed line in **a,d** and **e** corresponds to a distance of 10 mm.

polynomial growth with longer time to reach the stopping condition, while volume growth resulted in exponential growth (Extended Data Fig. 8). The faster growth rate in volume growth models means

a large contribution of parental clone to overall tumour growth and shorter time for advantageous subclones to outgrow and compete, leading to tumours with limited diversification.





**Early indication of evolutionary potential.** We have previously shown that evolutionary features correlate with clinical outcomes and could be used to guide patient management<sup>7</sup>. Therefore, it is of particular interest to examine whether the computational model could be used to suggest predictive features for the likely evolutionary trajectories and therefore clinical behaviour of individual tumours.

Of note, early-stage tumours under distinct growth modes appeared indistinguishable with respect to the number of subclones (Fig. 5a). We specifically investigated features that could indicate subsequent subclonal diversification in the surface growth model and noted the appearance and outgrowth of budding structures (Fig. 5d). Notably, as the tumour grew with gained fitness, the contour circularity of a tumour slice initially decreased and then recovered, concomitant with the initial increase and subsequent reduction in clonal diversity, respectively (Fig. 5e). Exploratory simulations attempting at ‘replaying’ evolution (that is, re-simulating clonal evolution from a historical tumour state with established clonal structure as a starting point) starting from different tumour sizes suggested that evolution was more repeatable if starting from a historical tumour state with budding structures emerging (Supplementary Note 7 and Extended Data Figs. 9 and 10).

With respect to the above findings, the radiological features of 46 tumours with diameter <7 cm in the TRACERx Renal study were evaluated (Supplementary Table 4). By qualitative examination of radiological images, budding structures were apparent at the surface of 16 tumours and evident in the tumour *ex vivo* (one representative, K523, is shown in Fig. 5f,g). In this case, adjacent to the budding structures were regions with high clonal diversity, consistent with surface growth models. Interestingly, the presence of budding in these 16 sub-7-cm tumours exhibiting increasing diversity as a function of tumour size, combined with the absence of budding and low diversity in some larger tumours (Fig. 5h), showed clear concordance with the temporal trend of clonal diversification and morphological variation observed in the surface growth models. The failure of this trend to continue in larger tumours supports the observed collapse of subclonal diversity in simulated tumours under surface growth.

## Discussion

Genetic ITH arises when clonally related populations of cells in the tumour acquire distinct genomic alterations, endowing the subclones with a range of fitness advantages. Our understanding of how major subclones sculpt evolutionary trajectories has been gleaned primarily from multi-region sampling and deep sequencing. However, our understanding of the temporal features of clonal evolution and our ability to predict evolutionary trajectories remain limited. Therefore, we focus on spatial and temporal characterization of clonal diversity to elucidate predictive features for

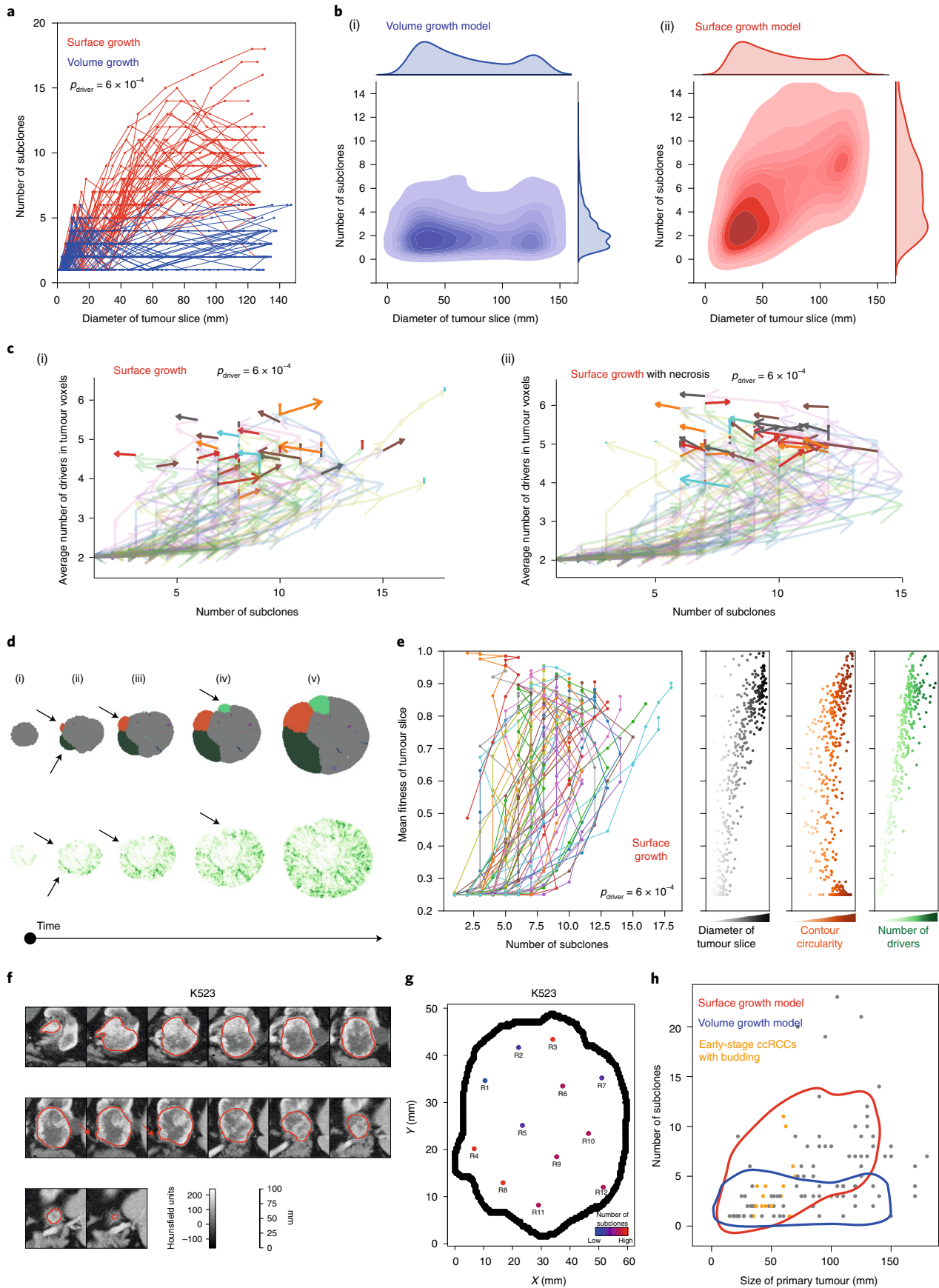
evolutionary potential, summarized in Fig. 6. To this end, we developed an agent-based model to study tumour growth and clonal evolution, with a focus on examining the contribution of different modes of growth, namely surface and volume growth, and the presence or absence of central necrosis to spatial and temporal features of clonal diversity.

Adding to previous modelling work on spatial elements of tumour growth<sup>24–27,33–37</sup>, our model demonstrates that growth modes impact subclonal diversification. Specifically, volume growth resulted in either limited evidence of evolution or punctuated evolution with early fixation of a fit clone, whereas surface growth gave rise to branched evolution with extensive subclonal diversification (Fig. 6). Intriguingly, surface growth models revealed a non-monotonic variation in clonal diversity over time with a dramatic collapse of diversity at large tumour sizes, consistent with the apparent relationship between static data of tumour size and clonal diversity in the TRACERx Renal study. These temporal features of clonal diversity informed by the model raise the possibility that evolutionary modes are not a static property but instead can undergo a dynamic switch from a branched to an apparently punctuated sub-type, with peak diversity occurring in the past, during tumour development.

Spatial analyses further uncovered that microdiversity hotspots and youngest subclones were more uniformly distributed in volume growth models while predominantly near the tumour margin in surface growth models (Fig. 6). As in the model, the spatial distribution of microdiversity hotspots exhibited a power-law pattern in ccRCCs. Strikingly, the exponent of the power law was associated with previously described different classes of ccRCC evolution. Tumours with attenuated progression had a larger exponent, which is consistent with their more branched phylogenetic trees. Both indolent mono-driver and aggressive poly-driver tumours had lower exponents, suggesting volume growth patterns, with the aggressive tumours simply determined in our model by the early acquisition of multiple strong drivers.

Investigation on the impact of necrosis in our model further broadened our understanding of the spatial and temporal features of clonal diversification. (Fig. 6). Incorporation of necrosis led to enhanced fitness in the tumour interior, suggestive of selection of fitter clones, in keeping with our recent study<sup>29</sup>. Furthermore, with necrosis, tumours under surface growth harboured additional microdiversity hotspots and youngest subclones at the centre. The pattern of youngest subclones was corroborated by the analysis of sequencing data and further supported by histological evidence of interface between tumour and acellular areas, suggesting that surface growth with necrosis incorporated could explain the evolution of some ccRCCs. Our recent work in the context of TRACERx Renal demonstrated that metastasis-competent subclones are enriched at the tumour centre, suggesting that environmental factors favoured their selection, possibly through acquisition of advantageous traits

**Fig. 5 | Growth modes impact the temporal features of clonal diversification.** **a**, Number of subclones as a function of the diameter of a 2D tumour slice in *in silico* tumours under surface growth and volume growth, for  $n = 50$  simulations with  $p_{\text{driver}} = 6 \times 10^{-4}$  for each condition. **b**, KDE with respect to the number of subclones and the diameter of a 2D tumour slice in *in silico* tumours under volume growth (i) and surface growth (ii). Each KDE plot is based on 250 simulations (50 per condition) under five conditions with  $p_{\text{driver}} = 2 \times 10^{-4}, 4 \times 10^{-4}, 6 \times 10^{-4}, 8 \times 10^{-4}$  and  $1 \times 10^{-3}$ . **c**, Vector maps of evolutionary flows over time with respect to the number of subclones and the average number of drivers accumulated among tumour voxels in surface growth models without (i) or with (ii) the implementation of necrosis.  $n = 50$  simulations with  $p_{\text{driver}} = 6 \times 10^{-4}$  are shown. **d**, The spatial patterns of parallel mutations in *PBRM1* (upper, distinct events in different colours) and microdiversity (lower) over time in a representative *in silico* tumour under surface growth. The arrows indicate budding structures preceding subclonal expansion. **e**, Time evolution with respect to the number of subclones and the mean fitness of the tumour slice, along with the diameter of tumour slice, contour circularity and average number of drivers accumulated, in surface growth models.  $n = 50$  simulations with  $p_{\text{driver}} = 6 \times 10^{-4}$  are shown. **f**, Axial image in the corticomedullary contrast phase of a representative case (K523) showing budding structure on the tumour surface (red arrow). Outlines in red reflect the tumour contour giving volumetric tumour coverage. **g**, Maps of tumour regions with the number of subclones colour coded in a representative case. Hues from red to purple to blue reflect decreasing number of subclones. ‘Low’ and ‘High’ reflect one and four subclones, respectively. **h**, The number of subclones as a function of ultimate tumour size in the TRACERx Renal study, overlaid with KDE based on simulated data. Tumours with size up to 7 cm and with radiologically evident budding structures are highlighted (orange). Contours reflect 90% probability density based on *in silico* tumours under surface growth (red) and volume growth (blue) in Fig. 6b.



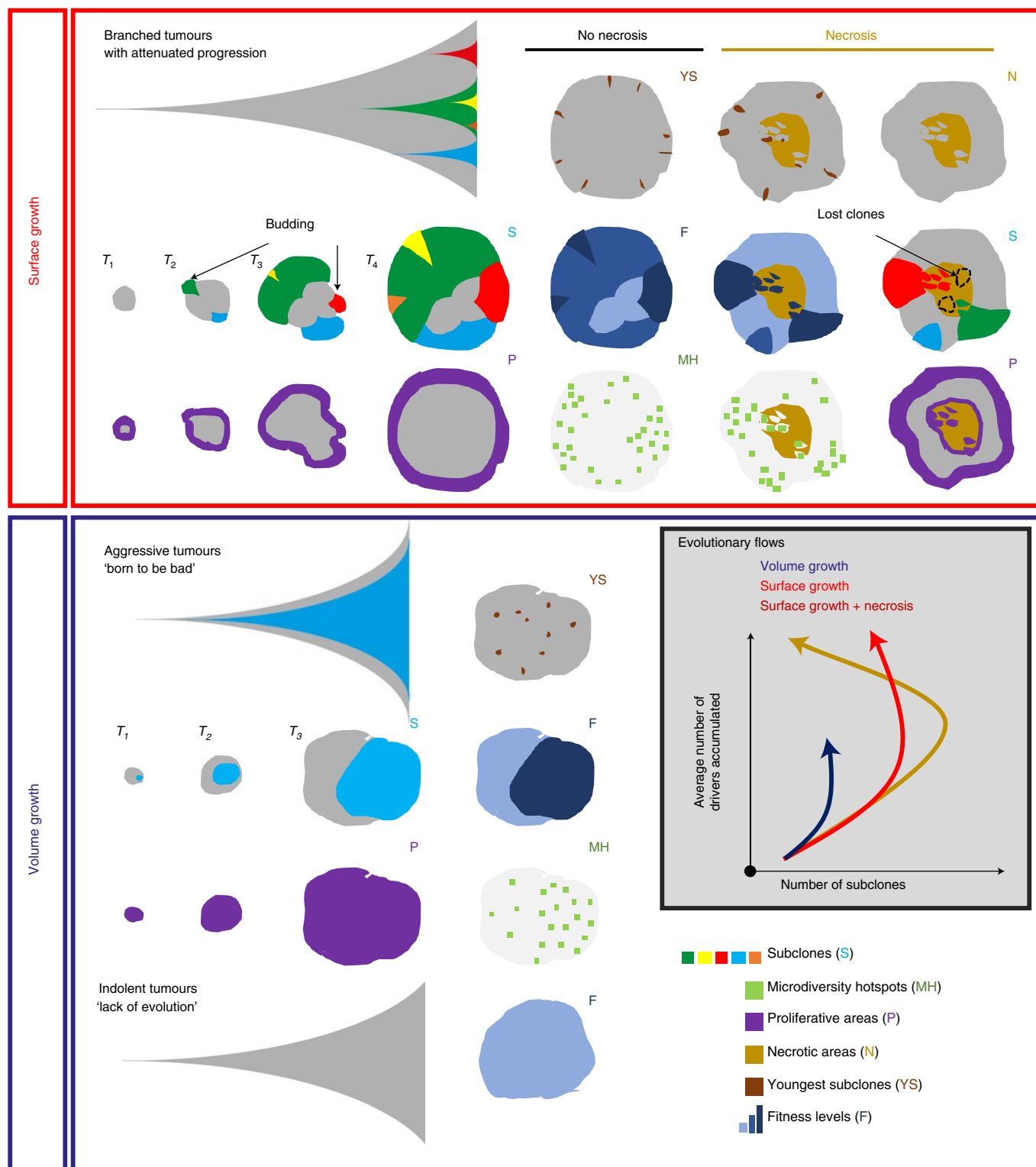


**Fig. 6 | Summary diagram: tumour growth modes impact the extent, spatial features and temporal trajectories of clonal diversification.** Surface growth models lead to attenuated progression with extensive subclonal diversification, reflective of branched evolution. At the early stage, the birth and outgrowth of proliferatively advantageous subclones causes the formation of surface budding structures and consequently a distorted tumour contour. As these subclones grow to collectively constitute the tumour frontier at a later stage, the tumour contour returns to a more circular shape with enrichment of youngest subclones and microdiversity hotspots and enhancement of fitness near the tumour margin. The incorporation of central necrosis causes the loss of macrodiversity but at the same time permits continued subclonal diversification in the tumour interior, evidenced by the enrichment of youngest subclones and microdiversity hotspots. In contrast, volume growth models give rise to dichotomous patterns of tumour growth and clonal evolution, developing tumours that are either indolent with 'lack of evolution' or aggressive with early birth of fitter subclone and rapid progression. The distributions of youngest subclones, microdiversity hotspots and fitness in volume growth models are more uniform than those in surface growth models.

such as epithelial-to-mesenchymal transition. In the current study, we present a complementary, and non-exclusive, perspective that necrosis could accelerate the rate of evolution, via turnover of tumour mass, to achieve enhanced fitness in the tumour centre.

Finally, tracking advantageous subclones over time in silico illuminated the rapid increase of their prevalence in small tumours, marked by the appearance of budding structures, concomitant with subclonal diversification in surface growth models. Intriguingly, budding structures were radiologically apparent in 16 early-stage ccRCC tumours, a subset of which already showed high clonal diversity, by molecular profiling. While budding structures in our model arose from advantageous subclonal outgrowth, alternative mechanisms cannot be excluded<sup>33,38</sup>.

To conclude, we have developed a model that enables us to understand how spatial patterns of growth and necrosis determine patterns of clonal diversity in space and time (Fig. 6). We validate our findings using patient data, thereby opening the potential for predicting future clinical behaviour, precision medicine's holy grail.

## Methods

**Computational model.** Tumour growth and clonal evolution in a spatio-temporal context have increasingly been studied with the aid of computational models that incorporate spatial elements of tumour growth and acquisition of genomic alterations<sup>24,25,33,34</sup>. Spatial patterns of tumour growth<sup>24–27</sup> have been shown to impact the ability to classify neutral evolution in contrast to selection, suggesting that spatial growth of a structured population interplays with evolutionary forces (driver acquisition, selection and genetic drift) to shape the spatial patterning of subclones.

In the present study, to establish an understanding of the spatial and temporal features of clonal diversification and to enhance the ability to predict evolutionary trajectories in ccRCC, we constructed a coarse-grained cellular automaton model to simulate tumour growth and clonal evolution. A basic model unit reflects a tumour volume of  $1 \times 1 \times 1 \text{ mm}^3$ , referred to as a 'tumour voxel'. The full simulation lattice comprises  $200 \times 200 \times 200$  lattice sites, each of which can accommodate a single tumour voxel when a tumour grows. As a simulation proceeds, tumour voxels stochastically undergo growth, death and acquisition of driver events upon growth (Extended Data Fig. 3). The subsequent sections detail the model components and assumptions.

**Growth and death.** Tumour voxels stochastically undergo growth and death, with baseline probabilities per simulation step of  $p_{\text{growth}} = 0.25$  and  $p_{\text{death}} = 0.05$ , respectively. Upon death, a tumour voxel is removed from the simulation lattice, rendering the site empty and available for accommodating new tumour voxels. Two different modes of spatial tumour growth are considered: surface growth and volume growth (Fig. 1c). For surface growth, proliferation only takes place when space is available, namely when at least 1 of the 26 neighbouring lattice sites of the tumour voxel selected to divide is empty. Upon duplication of a parent tumour voxel, one child tumour voxel retains the position of the parent while the other is placed at a randomly selected adjacent empty site. For volume growth, all tumour voxels can proliferate. Upon duplication, one child tumour voxel retains the position of the parent while the other is placed at a selected adjacent site according to the rule described below and pushes tumour voxels in that orientation outward. The process for selecting an adjacent site includes two steps: (1) random sampling of 10 candidate positions out of the 26 neighbouring lattice sites and (2) selection of the orientation (that is, pointing from the position of the parent tumour voxel to the candidate position) giving the smallest distance from the tumour surface, similar to the algorithm described in ref.<sup>24</sup>.

**Driver events.** A panel of 26 ccRCC drivers that were highlighted previously<sup>7</sup>, including mutations in 12 genes and 14 SCNAs, are considered in the present work (Extended Data Fig. 1). For simplicity, the selective advantage conferred by a driver is assumed to manifest as growth advantage.

Two ways of implementing selective advantages are considered and referred to as 'saturated' and 'additive' driver advantage models. In the saturated driver advantage model, the  $p_{\text{growth}}$  of a tumour voxel can be at one of three levels  $\{p_{\text{growth}}^{(\text{initial})}, p_{\text{growth}}^{(\text{moderate})}, p_{\text{growth}}^{(\text{maximal})}\}$ . Each driver endows a tumour voxel with one of these growth probabilities, and the relative differences in selective advantage of drivers are assumed to reflect their association with the Ki67 score in tumour regions (Extended Data Fig. 1) and their frequencies in the clinical cohort<sup>7</sup>.

In a general form,  $p_{\text{growth}}^{(\text{moderate})} = g(s)p_{\text{growth}}^{(\text{initial})}$  and  $p_{\text{growth}}^{(\text{maximal})} = h(s)p_{\text{growth}}^{(\text{initial})}$  are functions of the baseline growth probability, where  $h(s) \geq g(s) \geq 1$  reflect the growth advantages relative to the baseline. As one specific implementation,  $p_{\text{growth}}^{(\text{initial})} = 0.25$ ,  $p_{\text{growth}}^{(\text{moderate})} = (1 + s)p_{\text{growth}}^{(\text{initial})}$  and  $p_{\text{growth}}^{(\text{maximal})} = (1 + s)^2 p_{\text{growth}}^{(\text{initial})}$ ,

where  $0 \leq s \leq 1$  reflects the selective advantage. For simplicity, individual driver gene mutations are assigned with  $p_{\text{growth}}^{(\text{initial})}$ , whereas four SCNAs with strong association with Ki67 score (7q gain, 20q gain, 4q loss and 8p loss) are assumed to be the strongest drivers assigned with  $p_{\text{growth}}^{(\text{maximal})}$  and therefore their acquisition would lead to the biggest increase in growth probability. Importantly, the saturated model is implemented with only two levels of selective advantage, and the growth probability of a tumour voxel becomes saturated at 1 if acquiring the strongest driver. In comparison, the additive driver advantage model has a more graduated implementation of selective advantage. In this implementation, each driver adds a certain amount of growth probability to the tumour voxel that acquires the driver, namely  $p_{\text{growth}} = p_{\text{growth}}^{(\text{initial})} + \sum_k p_{\text{growth}_k}$ , where  $p_{\text{growth}_k}$  reflects the amount of growth probability added by driver  $k$  (Extended Data Fig. 2).  $p_{\text{growth}}$  is set to 1 if the calculated probability exceeds 1. The amount  $p_{\text{growth}_k}$  varies between drivers, reflecting the different strengths of their association with the Ki67 score (Extended Data Fig. 1). Three different scenarios were explored to reflect different amounts of growth probability endowed by drivers on average, as determined by the  $s_k$  of the weakest driver, namely  $\min(s_k)$ , and the difference in  $s_k$  between consecutive two drivers in their advantages, namely  $\Delta s_k$  (Extended Data Fig. 2).

Upon proliferation of a parent tumour voxel, child tumour voxels inherit existing driver events harboured by the parent tumour voxel and stochastically acquire new drivers. Individual driver gene mutations are assumed to be acquired with a greater probability ( $p_{\text{driver}}$ ) than SCNAs ( $0.001p_{\text{driver}}$ ). A second mutation in the same gene is assumed to never occur in the same tumour voxel, but multiple independent, distinct mutations in the same gene may be acquired in parallel within a simulated tumour in different tumour voxels. As the majority of ccRCCs have clonal *VHL* inactivation events, in general and in the TRACERx Renal cohort<sup>7</sup>, the founder tumour voxel is assumed to harbour *VHL* inactivation together with 3p loss as a clonal event. The subpopulation of tumour voxels that only harbour these two events is referred to as the parental clone. Based on their association with a high weighted genome instability index in the data from the TRACERx Renal study<sup>7</sup>, and functional evidence<sup>31,32</sup>, mutations in *PBRM1* or *BAP1* are assumed to enhance the probability of SCNAs acquisition (to  $p_{\text{driver}}$ ). A range of driver acquisition probabilities have been studied to explore the impact on the patterns we investigate (see Supplementary Note 8 for considerations for the selection of  $p_{\text{driver}}$  values in the coarse-grained model). Mutations and acquisition of SCNAs are assumed to be proliferation dependent, implying that DNA replication and chromosome mis-segregation is the main source of genomic alterations. Lastly, the selective advantage endowed by a driver is assumed to be fixed, so the variation in driver advantage dependent on changing environments is not considered in the current study.

**Necrosis.** Building upon our previous work<sup>29</sup>, necrosis is implemented in a subset of model conditions to evaluate its impact on features of clonal diversification. Specifically, tumour voxels located at a distance greater than  $d_{\text{necrosis}} = 15 \text{ mm}$  from the tumour surface undergo death with a probability of  $p_{\text{necrosis}}$ . A probability of  $p_{\text{necrosis}} = 0.5$  is used in this study, in keeping with our previous work. Like the spontaneous death described above, upon necrosis-induced death, a tumour voxel is removed from the simulation lattice, rendering the site empty and available for accommodating new tumour voxels.

**Simulation.** The procedure for simulating events of death, proliferation and acquisition of driver events is illustrated in a flow diagram (Extended Data Fig. 3). Briefly, each simulation starts from a single tumour voxel (that is, founder tumour voxel) that harbours a *VHL* mutation and 3p loss as truncal events, placed at the centre of the lattice,  $(x_0, y_0, z_0)$ . During the evaluation of possible death events, for each of all tumour voxels alive,  $p_{\text{death}}$  is compared with a random number generated in the range  $[0, 1]$ . If  $p_{\text{death}}$  is larger, a death event occurs, resulting in the lattice site being freed to accommodate a newly born tumour voxel in the future. During the evaluation of possible proliferation events, for each of all valid tumour voxels (see above for the difference between surface growth and volume growth),  $p_{\text{growth}}$  is determined according to the driver events harboured (see above for the difference between 'saturated' and 'additive' models of fitness advantage) and compared with a random number generated in the range  $[0, 1]$ . If  $p_{\text{growth}}$  is larger, a proliferation event occurs, resulting in a new tumour voxel being created nearby. During the evaluation of possible acquisition of driver events, for each of all the daughter tumour voxels just arising from proliferation and for each of the ccRCC drivers,  $p_{\text{driver}}$  is compared with a random number generated in the range  $[0, 1]$ . If  $p_{\text{driver}}$  is larger and that driver is not currently harboured by the tumour voxel, acquisition of the driver takes place in the given tumour voxel. In a subset of simulations, necrosis is implemented. During the evaluation of necrotic death events, for each of all tumour voxels alive, if it is located at a distance greater than  $d_{\text{necrosis}}$  from the tumour surface,  $p_{\text{necrosis}}$  is compared with a random number generated in the range of  $[0, 1]$ . If  $p_{\text{necrosis}}$  is larger, a necrotic death event occurs, resulting in the lattice site being freed to accommodate a newly born tumour voxel in the future. The simulation runs until the tumour grows to at least 1 million tumour voxels after the last simulation step. The computer code is written in CUDA C++.



**Evolutionary replay.** The procedure for simulating evolutionary replay is illustrated in a flow diagram (Extended Data Fig. 9). Briefly, a preparation step is performed to create evolutionary snapshots of a simulated tumour at different timepoints. Specifically, each snapshot contains precise information about the positions, subclone identities and drivers of all tumour voxels. At the beginning of evolutionary replay,  $N$  replicate tumours are reconstructed, each with a copy of the same evolutionary snapshot at a given timepoint  $t$ . Then, these replicate tumours undergo the events described above, each with a different unique random seed, and grow to the predefined stopping size. Evolutionary outcomes from these replicate tumours are evaluated and compared.

**Model analyses. Levels of analysis.** Analyses are conducted at three different levels (Fig. 1d): (1) the whole-tumour level, which takes into account all tumour voxels in the three-dimensional (3D) volume, (2) the tumour slice level, which takes into account all tumour voxels within a two-dimensional (2D) plane ( $z = z_0$ ) and (3) the regional biopsy level, which takes into account tumour voxels within regional biopsies. A regional biopsy is defined as all tumour voxels within a region in the 2D slice. Spatially uniform sampling is performed in this study. This process is carried out by locating the centres of candidate regional biopsies in the  $200\text{ mm} \times 200\text{ mm}$  2D lattice with a spacing of 20 mm and collecting all voxels within a distance of 5 mm from each biopsy centre.

**CCF of subclones.** The CCF of a subclone is calculated as the number of tumour voxels that belong to a subclone divided by the total number of tumour voxels in the domain of interest, depending on the level of analysis. A subclone is identified by a set of driver events, shared by a subpopulation of tumour voxels, which are accumulated within the subclone-initiating tumour voxel. A subclone-initiating tumour voxel is defined as a tumour voxel that acquires a new driver event upon birth. A subclone is considered detectable if the CCF is greater than 0.01.

**Shannon diversity index.** As a measure of clonal diversity, the Shannon diversity index is defined as  $S = -\sum f_i \ln f_i$ , where  $f_i$  is the CCF of subclone  $i$ . All subclones are considered in this calculation.

**Number of drivers accumulated.** The drivers (including both mutations and SCNAs) harboured by each tumour voxel within a tumour slice are counted at each timepoint. The average number of drivers among all tumour voxels is then calculated.

**Fitness.** The fitness of a tumour voxel is defined as the instantaneous growth probability,  $P_{\text{growth}}$ , dependent on the set of drivers harboured by that tumour voxel. In representative cases, the fitness of tumour voxels is mapped within a 2D tumour slice. To examine the spatial features of tumour fitness, the distances from every tumour voxel to the centre of a tumour slice and to the nearest point along the tumour contour are calculated, respectively. The central-most 10% of tumour voxels, with the shortest distances to the centre, and the marginal-most 10% of tumour voxels, with the shortest distances to the margin, are sampled to calculate a sample-average fitness. Additionally, another 10% of tumour voxels is randomly sampled for comparison. The ratio of the mean fitness of the central-most 10% of tumour voxels to that of the marginal-most 10% of tumour voxels, denoted as 'Ratio\_C2M', is calculated for each simulation.

**Microdiversity.** Microdiversity is defined as the number of subclones contained in a  $3 \times 3\text{ mm}^2$  region within the tumour slice. In representative cases, microdiversity is spatially mapped within a tumour slice, by sliding a  $3 \times 3\text{ mm}^2$  spatial window throughout the tumour slice. Microdiversity hotspots are defined as a subset of these small regions with five or more subclones. The distance from a microdiversity hotspot to the centre of a tumour slice is referred to as the distance to tumour centre ( $d_1$ ). The distance from a microdiversity hotspot to the nearest point along the tumour contour is referred to as the distance to tumour margin ( $d_2$ ). The normalized distance to tumour centre is defined as  $d = d_1/(d_1 + d_2)$ . The cumulative probability distribution,  $P(D \leq d)$ , of  $d$  is generated by combining microdiversity hotspots from repeat simulations. The power-law exponent is obtained by bootstrapping 100 samples of 400 hotspots per sample and fitting a power-law function to the cumulative probability distribution of  $d$  in each sample.

**Youngest subclones.** Youngest subclones are defined as the subclones that emerge closest to the end of a simulation. For the analysis of their spatial distribution, we recorded the 100 youngest subclones within a 2D tumour slice and, for each of them, measured the distance from its position to the tumour margin. The mean of the distances for these 100 subclones was calculated for comparison between different replicate simulations.

**Contour circularity.** Tumour contours are determined from 2D tumour slices. Smoothing is performed for each tumour voxel along the tumour contour by calculating the mean  $(x, y)$  position of this tumour voxel and adjacent tumour voxels. After smoothing, contour circularity is calculated as  $\text{Circularity} = \frac{4\pi \text{Area}}{\text{Perimeter}^2}$ .

**Temporal analysis.** For the time-course study, 2D tumour slices are collected over multiple timepoints. The number of subclones is counted within each historical

tumour slice. Kernel density estimation (KDE) with a Gaussian kernel is performed with respect to the number of subclones and the diameter of the tumour slice, based on all simulations under a given model condition, to produce a continuous density estimate.

**Analyses of tumour data. TRACERx Renal cohort.** Seventy-nine tumour sections of 66 unique primary tumours are included in this study. See the exclusion criterion in our previous publication<sup>29</sup>.

**Computed tomography images.** Contrast-enhanced computed tomography images were obtained using standard-of-care imaging sequences in 91 patients and curated using a local research picture archiving and communication system based on the Extensible Neuroimaging Archive Toolkit platform<sup>39</sup>. Outlines were drawn by consensus between an oncologist (S.T.C.S.) and a radiologist (D.A.), giving volumetric tumour coverage, from which image strips were prepared for rapid visualization of all tumour slices for all patients using an in-house script written in Python.

To detect presence or absence of budding structures in the contoured CT data, qualitative assessment of contoured tumours was performed by X.F. and S.T.C.S. and verified by a radiologist (D.A.).

**Histological analysis.** Haematoxylin and eosin-stained histological sections of representative cases were evaluated by two pathologists (J.I.L. and C.E.S.). Each sample was qualitatively assessed for the relative amount of viable tumour cells, fibrosis and presence of necrosis.

**Microdiversity.** Spatial maps of regional clone diversity are created for two representative tumour sections. In these maps, regions are colour coded based on the number of subclones. Regions that harbour at least one subclone are treated as a proxy for microdiversity hotspots defined in the model analysis. In total, there are 606 regions from 54 tumours that satisfy this criterion. In evaluation of association between microdiversity features and clinical annotations, subsets of tumours are considered. Subsets with different relapse statuses consist of 270 ('relapse') and 336 regions ('no relapse'), respectively. Subsets with different rates of disease progression consist of 276 ('no progression'), 265 ('attenuated progression') and 65 regions ('rapid progression'), respectively. For tumour regions, the normalized distance to tumour centre is measured as described above in Model analyses section.

**Parallel evolution.** Spatial maps of parallel mutational events in *PBRM1* and *BAP1*, respectively, are created for two representative tumours. In these maps, regions are coloured differently according to different parallel mutational events. Regions that harbour more than one event are indicated with multiple colours. To study the spatial distribution of mutational events with limited clonal expansion, the maximum distance from an event spanning a single region to the tumour margin is measured.

**Statistical analysis.** The two-sided Wilcoxon's rank test was performed to compare a particular measurement between different conditions. Statistical significance is annotated within box plots using `stat_compare_means` (method = 'wilcox.test', label = 'p.signif') in R.

Bootstrapping was performed to generate 100 random samples of 400 microdiversity hotspots per sample with replacement, using `random.choice()` in Python. The power-law exponent was then determined by fitting a power-law function to the cumulative probability distribution from each sample, using `scipy.optimize.curve_fit()` in Python.

The quantile–quantile (Q–Q) plot was generated to compare the actual distribution of microdiversity hotspots with a power-law distribution with the exponent as the median of fitted values in bootstrapping, using `statsmodels.graphics.gofplots.qqplot()` in Python.

KDE was performed for simulations with respect to the size of tumour slice and the number of subclones, using `seaborn.jointplot` (kind = 'kde') in Python.

R v.3.6.2 and Python v.3.7.7 were used for these analyses.

**Reporting Summary.** Further information on research design is available in the Nature Research Reporting Summary linked to this article.

## Data availability

Multi-region sequencing data that support the analysis in this study were published in the previous TRACERx Renal study<sup>7</sup> and are deposited in the European Genome-Phenome Archive <https://ega-archive.org/studies/EGAS00001002793>. Data on spatial features of microdiversity and parallel evolution and characterization of budding structures in tumours are provided in the Supplementary Tables. Source data are provided with this paper and are available on GitHub repositories <https://github.com/FrancisCrickInstitute/tumour-growth-patterns-impact-evolution> and <https://github.com/iamfuxiao/tumour-growth-patterns-impact-evolution><sup>40</sup>.

## Code availability

CUDA C++ computer code developed for the study and analysis scripts for generating figures are available on GitHub repositories <https://github.com/FrancisCrickInstitute/tumour-growth-patterns-impact-evolution> and <https://github.com/iamfuxiao/tumour-growth-patterns-impact-evolution><sup>40</sup>.

Received: 15 February 2021; Accepted: 7 October 2021;  
Published online: 23 December 2021

## References

- Merlo, L. M. F., Pepper, J. W., Reid, B. J. & Maley, C. C. Cancer as an evolutionary and ecological process. *Nat. Rev. Cancer* **6**, 924–935 (2006).
- Zahir, N., Sun, R., Gallahan, D., Gatenby, R. A. & Curtis, C. Characterizing the ecological and evolutionary dynamics of cancer. *Nat. Genet.* **52**, 759–767 (2020).
- McGranahan, N. & Swanton, C. Clonal heterogeneity and tumor evolution: past, present, and the future. *Cell* **168**, 613–628 (2017).
- Gerlinger, M. et al. Intratumor heterogeneity and branched evolution revealed by multiregion sequencing. *N. Engl. J. Med.* **366**, 883–892 (2012).
- Yates, L. R. et al. Subclonal diversification of primary breast cancer revealed by multiregion sequencing. *Nat. Med.* **21**, 751–759 (2015).
- Jamal-Hanjani, M. et al. Tracking the evolution of non-small-cell lung cancer. *N. Engl. J. Med.* <https://doi.org/10.1056/NEJMoa1616288> (2017).
- Turajlic, S. et al. Deterministic evolutionary trajectories influence primary tumor growth: TRACERx Renal. *Cell* <https://doi.org/10.1016/j.cell.2018.03.043> (2018).
- McGranahan, N. & Swanton, C. Biological and therapeutic impact of intratumor heterogeneity in cancer evolution. *Cancer Cell* **27**, 15–26 (2015).
- Lopez, J. I. & Cortes, J. M. A divide-and-conquer strategy in tumor sampling enhances detection of intratumor heterogeneity in routine pathology: a modeling approach in clear cell renal cell carcinoma. *F1000Research* **5**, 1–14 (2016).
- Mengelbier, L. H. et al. Intratumoral genome diversity parallels progression and predicts outcome in pediatric cancer. *Nat. Commun.* **6**, 6125 (2015).
- Casasent, A. K. et al. Multiclonal invasion in breast tumors identified by topographic single cell sequencing. *Cell* **172**, 205–217.e12 (2018).
- Melchor, L. et al. Single-cell genetic analysis reveals the composition of initiating clones and phylogenetic patterns of branching and parallel evolution in myeloma. *Leukemia* **28**, 1705–1715 (2014).
- Murugaesu, N. et al. Tracking the genomic evolution of esophageal adenocarcinoma through neoadjuvant chemotherapy. *Cancer Discov.* **5**, 821–832 (2015).
- Voss, M. H. et al. Tumor genetic analyses of patients with metastatic renal cell carcinoma and extended benefit from mTOR inhibitor therapy. *Clin. Cancer Res.* **20**, 1955–1964 (2014).
- Juric, D. et al. Convergent loss of PTEN leads to clinical resistance to a PI(3)K $\alpha$  inhibitor. *Nature* **518**, 240–244 (2015).
- Watkins, T. B. K. et al. Pervasive chromosomal instability and karyotype order in tumour evolution. *Nature* **587**, 126–132 (2020).
- Bassez, A. et al. A single-cell map of intratumoral changes during anti-PD1 treatment of patients with breast cancer. *Nat. Med.* **27**, 820–832 (2021).
- Cresswell, G. D. et al. Mapping the breast cancer metastatic cascade onto ctDNA using genetic and epigenetic clonal tracking. *Nat. Commun.* <https://doi.org/10.1038/s41467-020-15047-9> (2020).
- Abbosh, C. et al. Phylogenetic ctDNA analysis depicts early-stage lung cancer evolution. *Nature* **545**, 446–451 (2017).
- Woodcock, D. J. et al. Prostate cancer evolution from multilineage primary to single lineage metastases with implications for liquid biopsy. *Nat. Commun.* **11**, 5070 (2020).
- Kingston, B. et al. Genomic profile of advanced breast cancer in circulating tumour DNA. *Nat. Commun.* **12**, 2423 (2021).
- Rodriguez-Brenes, I. A., Komarova, N. L. & Wodarz, D. Tumor growth dynamics: insights into evolutionary processes. *Trends Ecol. Evol.* **28**, 597–604 (2013).
- Gerlee, P. The model muddle: in search of tumor growth laws. *Cancer Res.* **73**, 2407–2411 (2013).
- Sun, R. et al. Between-region genetic divergence reflects the mode and tempo of tumor evolution. *Nat. Genet.* **49**, 1015–1024 (2017).
- Chkhaidze, K. et al. Spatially constrained tumour growth affects the patterns of clonal selection and neutral drift in cancer genomic data. *PLOS Comput. Biol.* <https://doi.org/10.1101/544536> (2019).
- Noble, R., Burri, D., Kather, J. N. & Beerenwinkel, N. Spatial structure governs the mode of tumour evolution. Preprint at *bioRxiv* <https://doi.org/10.1101/586735> (2019).
- West, J., Schenck, R. O., Gatenbee, C., Robertson-tessi, M. & Anderson, A. R. A. Normal tissue architecture determines the evolutionary course of cancer. *Nat. Commun.* **12**, 2060 (2021).
- Hoefflin, R. et al. Spatial niche formation but not malignant progression is a driving force for intratumoral heterogeneity. *Nat. Commun.* **7**, 11845 (2016).
- Zhao, Y. et al. Selection of metastasis competent subclones in the tumour interior. *Nat. Ecol. Evol.* **5**, 1033–1045 (2021).
- Turajlic, S. et al. Tracking cancer evolution reveals constrained routes to metastases: TRACERx Renal. *Cell* <https://doi.org/10.1016/j.cell.2018.03.057> (2018).
- Varela, I. et al. Exome sequencing identifies frequent mutation of the SWI/SNF complex gene PBRM1 in renal carcinoma. *Nature* **469**, 539–542 (2011).
- Peng, J. et al. Stabilization of MCRS1 by BAP1 prevents chromosome instability in renal cell carcinoma. *Cancer Lett.* **369**, 167–174 (2015).
- Anderson, A. R. A., Weaver, A. M., Cummings, P. T. & Quaranta, V. Tumor morphology and phenotypic evolution driven by selective pressure from the microenvironment. *Cell* **127**, 905–915 (2006).
- Waclaw, B. et al. A spatial model predicts dispersal and cell turnover cause reduced intra-tumor heterogeneity. *Nature* **525**, 261–264 (2015).
- Noble, R., Burley, J. T., Le Sueur, C. & Hochberg, M. E. When, why and how tumour clonal diversity predicts survival. *Evol. Appl.* **13**, 1558–1568 (2020).
- Ahmed, Z. & Gravel, S. Intratumor heterogeneity and circulating tumor cell clusters. *Mol. Biol. Evol.* **35**, 2135–2144 (2018).
- Antal, T., Krapivsky, P. L. & Nowak, M. A. Spatial evolution of tumors with successive driver mutations. *Phys. Rev. E* **92**, 1–8 (2015).
- Fiore, V. F. et al. Mechanics of a multilayer epithelium instruct tumour architecture and function. *Nature* <https://doi.org/10.1038/s41586-020-2695-9> (2020).
- Marcus, D. S., Olsen, T. R., Ramaratnam, M. & Buckner, R. L. The extensible neuroimaging archive toolkit an informatics platform for managing, exploring, and sharing neuroimaging data. *Neuroinformatics* **7**, 11–34 (2007).
- Fu, X. et al. Spatial patterns of tumour growth impact clonal diversification. *Figshare* <https://doi.org/10.25418/crick.17032406> (2021).

## Acknowledgements

This research was funded in whole, or in part, by the Wellcome Trust (FC001003). For the purpose of open access, the author has applied a CC BY public copyright licence to any author accepted manuscript version arising from this submission. This work was supported by the Francis Crick Institute, which receives its core funding from Cancer Research UK (FC001003, FC001144, FC001169 and FC001988), the UK Medical Research Council (FC001003, FC001144, FC001169 and FC001988) and the Wellcome Trust (FC001003, FC001144, FC001169 and FC001988). S.T. is funded by Cancer Research UK (grant reference number A29911); the Francis Crick Institute, which receives its core funding from Cancer Research UK (FC10988), the UK Medical Research Council (FC10988) and the Wellcome Trust (FC10988); the National Institute for Health Research (NIHR) Biomedical Research Centre at the Royal Marsden Hospital and Institute of Cancer Research (grant reference number A109), the Royal Marsden Cancer Charity, The Rosetrees Trust (grant reference number A2204), Ventana Medical Systems Inc (grant reference numbers 10467 and 10530), the National Institute of Health (U01 CA247439) and Melanoma Research Alliance (award reference no. 686061). S.T. has received speaking fees from Roche, Astra Zeneca, Novartis and Ipsen. S.T. has the following patents filed: Indel mutations as a therapeutic target and predictive biomarker (PCTGB2018/051892 and PCTGB2018/051893) and Clear Cell Renal Cell Carcinoma Biomarkers (P113326GB). K.L. is funded by the UK Medical Research Council (MR/V033077/1), the Rosetrees Trust and Cotswold Trust (A2437), the Royal Marsden Cancer Charity, Melanoma Research Alliance (award reference no. 686061) and Cancer Research UK (C69256/A30194). C.S. is Royal Society Napier Research Professor (RP150154). C.S. is funded by Cancer Research UK (TRACERx, PEACE and CRUK Cancer Immunotherapy Catalyst Network), Cancer Research UK Lung Cancer Centre of Excellence (C11496/A30025), the Rosetrees Trust, Butterfield and Stonegate Trusts, NovoNordisk Foundation (ID16584), Royal Society Professorship Enhancement Award (RP/EA/180007), the National Institute for Health Research (NIHR) Biomedical Research Centre at University College London Hospitals, the Cancer Research UK-University College London Centre, Experimental Cancer Medicine Centre and the Breast Cancer Research Foundation (BCRF 20-157). This work was supported by a Stand Up To Cancer-LUNGevity-American Lung Association Lung Cancer Interception Dream Team Translational Research Grant (grant no. SU2C-AAACR-DT23-17 to S.M. Dubinett and A.E. Spira). Stand Up To Cancer is a division of the Entertainment Industry Foundation. Research grants are administered by the American Association for Cancer Research, the Scientific Partner of SU2C. C.S. is in receipt of an ERC Advanced Grant (PROTEUS) from the European Research Council under the European Union's Horizon 2020 research and innovation programme (grant agreement no. 835297). A.F. receives funding from the European Union's Horizon 2020 research and innovation programme under the Marie Skłodowska-Curie grant agreement no. 892360. We thank colleagues from the Biomolecular Modelling Lab, Tumour Cell Biology Lab, Cancer Dynamics Lab, and Cancer Evolution and Genome Instability Lab for insightful discussion and comments on this manuscript as well as the TRACERx Renal trial team and the Skin and Renal Unit Research Team at the Royal Marsden NHS Foundation Trust, including E. Carlyle, L. Del Rosario, K. Edmonds, K. Lingard, M. Mangwende, S. Sarker, C. Lewis, F. Williams, H. Ahmad, T. Foley, D. Kabir, J. Korteweg, A. Murra, N. Shaikh, K. Peat, S. Vaughan and L. Holt. TRACERx Renal is funded by NIHR BRC at the Royal Marsden Hospital and Institute of Cancer Research (A109) and the Francis Crick Institute, which receives its core funding from CRUK (FC010110), the UK Medical Research Council (FC010110) and the Wellcome Trust (FC010110).

## Author contributions

X.F., Y.Z., E.S., K.L., S.T. and P.A.B. conceived and designed the study. X.F. and P.A.B. constructed the computational model and performed simulations. Y.Z., C.E.S., K.L. and

S.T. provided the tumour samples and performed imaging analysis. S.J.D., M.R.O. and S.K. curated and processed the radiological data in this study. S.T.C.S. performed the initial outlining of the tumours, and D.A. checked and refined them. X.F. performed data analysis on simulations. X.F., Y.Z. and J.L.L. performed data analysis on tumour samples. All authors contributed data and to the interpretation of results. X.F., E.S., S.T. and P.A.B. wrote the manuscript with input from all authors.

### Competing interests

K.L., S.T. and C.S. have a patent on indel burden and checkpoint inhibitor response pending, and a patent on targeting of frameshift neoantigens for personalized immunotherapy pending. K.L. reports speaker fees from Roche Tissue Diagnostics, research funding from CRUK TDL/Ono/LifeArc alliance and a consulting role with Monopteros Therapeutics. S.T. reports grants from Ventana, outside the submitted work. J.L. reports institutional research support from BMS, MSD, Novartis, Pfizer, Achilles Therapeutics, Roche, Nektar Therapeutics, Covance, Immunocore, Pharmacylics and Aveo, and consultancy support from Achilles, AZ, Boston Biomedical, BMS, Eisai, EUSA Pharma, GSK, Ipsen, Imugene, Incyte, iOnctura, Kymab, Merck Serono, MSD, Nektar, Novartis, Pierre Fabre, Pfizer, Roche/Genentech, Secarna and Vitaccess. C.S. acknowledges grant support from Pfizer, AstraZeneca, Bristol Myers Squibb, Roche-Ventana, Boehringer-Ingelheim, Invitae (previously Archer Dx Inc) – collaboration in minimal residual disease sequencing technologies, and Ono Pharmaceutical, and is an AstraZeneca Advisory Board member and Chief Investigator for the MeRmaid1 and 2 clinical trials. C.S. has consulted for Amgen, Pfizer, Novartis, GlaxoSmithKline, MSD, Bristol Myers Squibb, Celgene, AstraZeneca, Illumina, Genentech, Roche-Ventana, GRAIL, Medicxi, Metabomed, Bicycle Therapeutics, Roche Innovation Centre Shanghai and the Sarah Cannon Research Institute. C.S. had stock options in Apogen Biotechnologies and GRAIL, has stock options in Epic Bioscience, and has stock options and is co-founder of Achilles Therapeutics. C.S. holds European patents relating to assay technology to detect tumour recurrence (PCT/GB2017/053289), to targeting neoantigens (PCT/EP2016/059401), identifying patent response to immune checkpoint blockade (PCT/EP2016/071471), determining HLA LOH (PCT/GB2018/052004), predicting survival rates of patients with cancer

(PCT/GB2020/050221), identifying patients who respond to cancer treatment (PCT/GB2018/051912), a US patent relating to detecting tumour mutations (PCT/US2017/28013) and both a European and US patent related to identifying insertion/deletion mutation targets (PCT/GB2018/051892). E.S. receives research support from AstraZeneca, Glaxo SmithKline and Merck Sharp & Dhome and is on the advisory board of Phenomic AI. The remaining authors declare no competing interests.

### Additional information

**Extended data** is available for this paper at <https://doi.org/10.1038/s41559-021-01586-x>.

**Supplementary information** The online version contains supplementary material available at <https://doi.org/10.1038/s41559-021-01586-x>.

**Correspondence and requests for materials** should be addressed to Erik Sahai, Kevin Litchfield, Samra Turajlic or Paul A. Bates.

**Peer review information** *Nature Ecology & Evolution* thanks Liang Cheng and the other, anonymous, reviewer(s) for their contribution to the peer review of this work.

**Reprints and permissions information** is available at [www.nature.com/reprints](http://www.nature.com/reprints).

**Publisher's note** Springer Nature remains neutral with regard to jurisdictional claims in published maps and institutional affiliations.



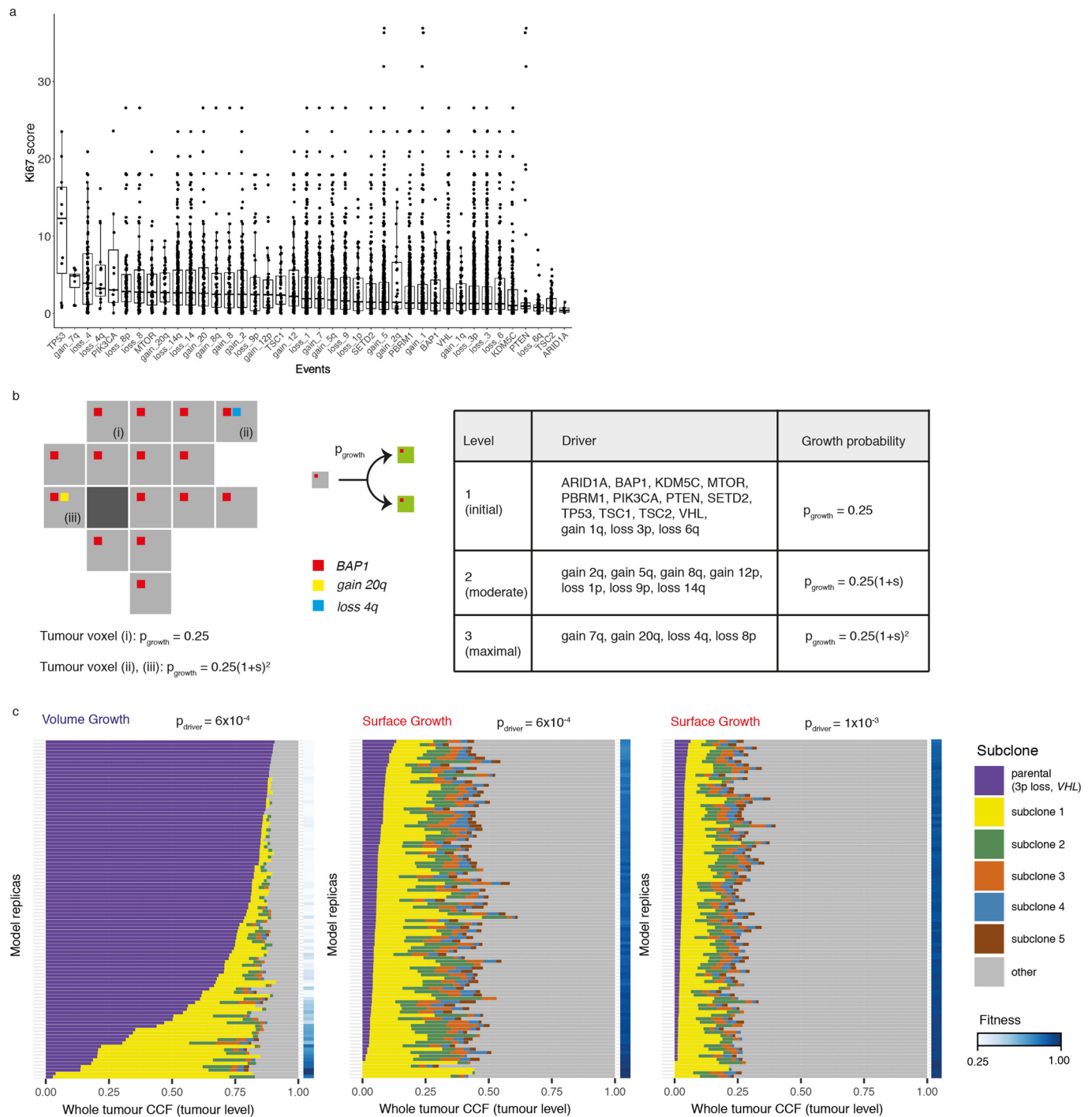
**Open Access** This article is licensed under a Creative Commons Attribution 4.0 International License, which permits use, sharing, adaptation, distribution and reproduction in any medium or format, as long as you give appropriate credit to the original author(s) and the source, provide a link to the Creative Commons license, and indicate if changes were made. The images or other third party material in this article are included in the article's Creative Commons license, unless indicated otherwise in a credit line to the material. If material is not included in the article's Creative Commons license and your intended use is not permitted by statutory regulation or exceeds the permitted use, you will need to obtain permission directly from the copyright holder. To view a copy of this license, visit <http://creativecommons.org/licenses/by/4.0/>.

© The Author(s) 2021

## on behalf of the TRACERx Renal Consortium

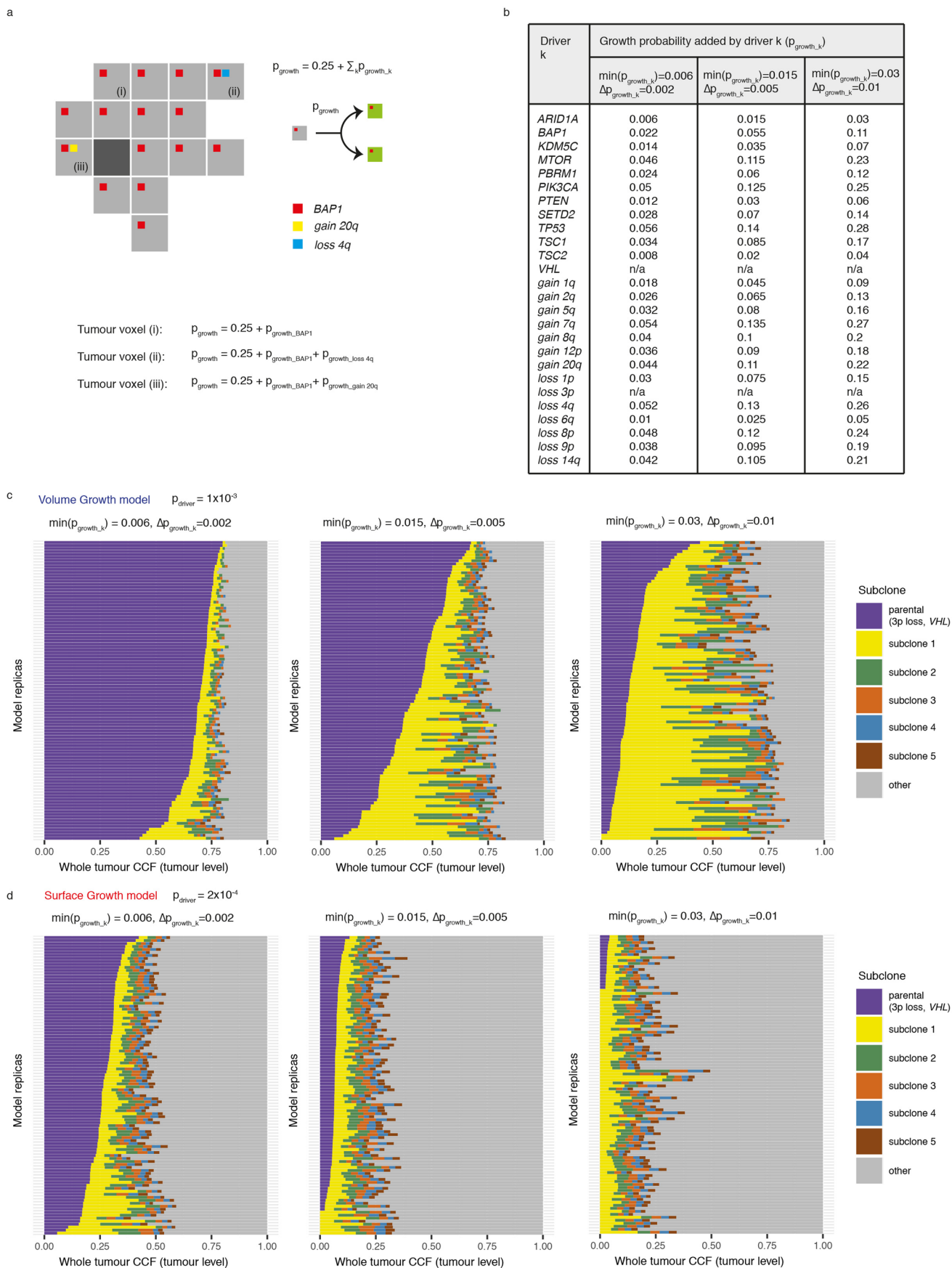
Lewis Au<sup>8,9</sup>, Ben Challacombe<sup>14</sup>, Ashish Chandra<sup>16</sup>, Simon Chowdhury<sup>17</sup>, William Drake<sup>25</sup>, Annika Fendler<sup>8</sup>, Archana Fernando<sup>14</sup>, Nicos Fotiadis<sup>26</sup>, Andrew J. S. Furness<sup>8,9</sup>, Emine Hatipoglu<sup>27</sup>, Karen Harrison-Phipps<sup>28</sup>, Steve Hazell<sup>10</sup>, Peter Hill<sup>29</sup>, Catherine Horsfield<sup>16</sup>, James Larkin<sup>9</sup>, Jose I. Lopez<sup>7</sup>, Teresa Marafioti<sup>30</sup>, David Nicol<sup>15</sup>, Tim O'Brien<sup>14</sup>, Jonathon Olsburgh<sup>14</sup>, Lisa Pickering<sup>9</sup>, Alexander Polson<sup>16</sup>, Sergio Quezada<sup>27</sup>, Sarah Rudman<sup>17</sup>, Scott T. C. Shepherd<sup>8,9</sup>, Charlotte E. Spencer<sup>8,9</sup>, Charles Swanton<sup>3,4,22</sup>, Samra Turajlic<sup>8,9</sup>, Mary Varia<sup>16</sup> and Hema Verma<sup>31</sup>

<sup>25</sup>Department of Endocrinology, St Bartholomew's Hospital, London, UK. <sup>26</sup>Department of Radiology, The Royal Marsden NHS Foundation Trust, London, UK. <sup>27</sup>Cancer Immunology Unit, Research Department of Haematology, University College London Cancer Institute, London, UK. <sup>28</sup>Thoracic Surgery and Otolaryngology – Head and Neck Surgery, Guy's and St Thomas' NHS Foundation Trust, London, UK. <sup>29</sup>Hammersmith Hospital, Imperial College Healthcare, London, UK. <sup>30</sup>Department of Cellular Pathology, University College London Hospitals, London, UK. <sup>31</sup>Department of Radiology, Guy's & St Thomas' NHS Foundation Trust, London, UK.



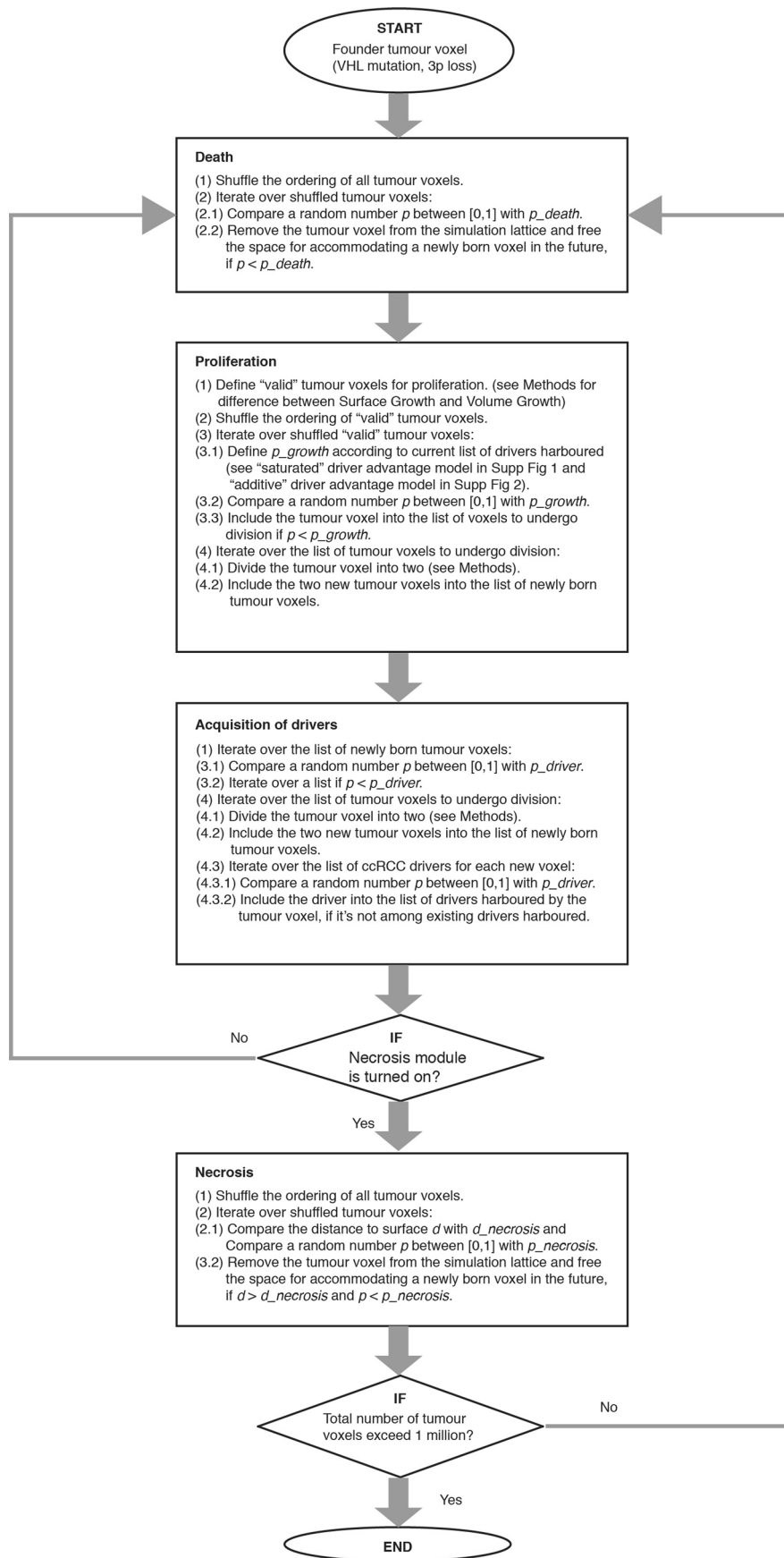
**Extended Data Fig. 1 | Saturated model of driver advantages.** (a) Ki67 immunohistochemistry (IHC) score in patient tumour (PT) regions where a particular driver is present. (b) Schematic figure of probabilistic growth of tumour voxels, with the growth probability of a tumour voxel defined by the strongest driver. (c) A table summarising the assumed levels of growth probabilities endowed by individual drivers. (d) Whole-tumour CCF of parental and largest subclones under Volume Growth (i) and Surface Growth (ii-iii), respectively. Average fitness in a tumour slice for each simulation is presented as a heat map. Driver acquisition probabilities in these sets of simulations are  $p_{\text{driver}} = 6 \times 10^{-4}$  in (i),  $6 \times 10^{-4}$  in (ii),  $1 \times 10^{-3}$  in (iii), respectively. 'Parental (3p loss, *VHL*)' clone is shown along with up to five subclones with a whole-tumour CCF of 0.01 or higher. All remaining subclones are represented in the 'other' group.





Extended Data Fig. 2 | See next page for caption.

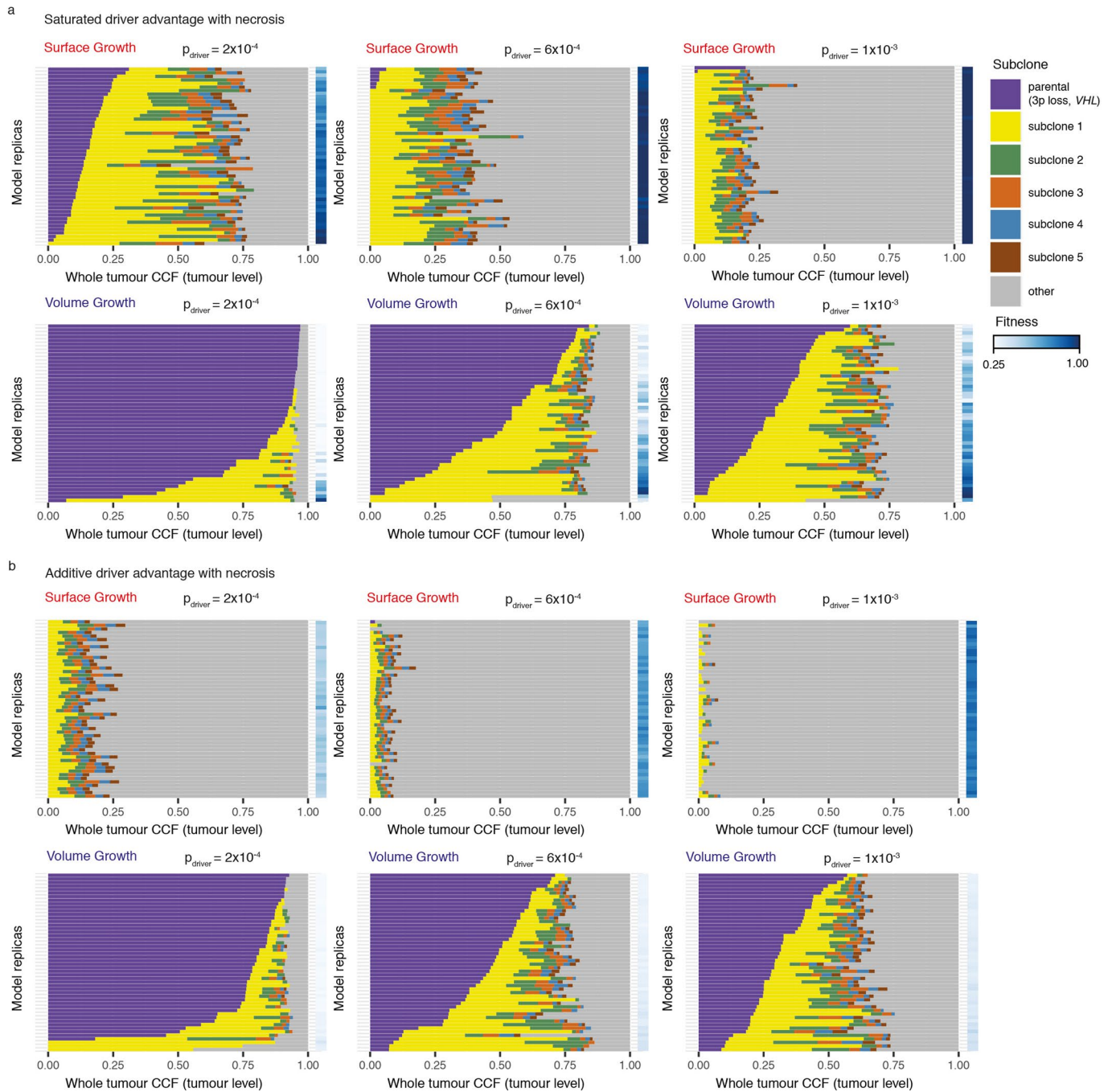
**Extended Data Fig. 2 | Additive model of driver advantages.** (a) Schematic figure of probabilistic growth of tumour voxels, with the growth probability of a tumour voxel cumulatively determined by the drivers harboured. (b) A table summarising the assumed amount of growth probabilities added by each driver ( $p_{growth\_k}$  for a driver  $k$ ). Three scenarios were explored, indicated in the table by  $p_{growth\_k}$  of the weakest driver, namely,  $\min(p_{growth\_k})$ , and the difference in  $p_{growth\_k}$  between consecutive two drivers as in the strength of their association with Ki67 IHC score, namely,  $\Delta p_{growth\_k}$ . (c-d) Whole-tumour cancer cell fraction (CCF) of parental and largest subclones in *in-silico* tumours under Volume Growth (c) and Surface Growth (d), respectively, under the indicated parameter conditions. 'Parental (3p loss, *VHL*)' clone is shown along with up to five subclones with a whole-tumour CCF of 0.01 or higher. All remaining subclones are represented in the 'other' group.  $N = 100$  for each condition.



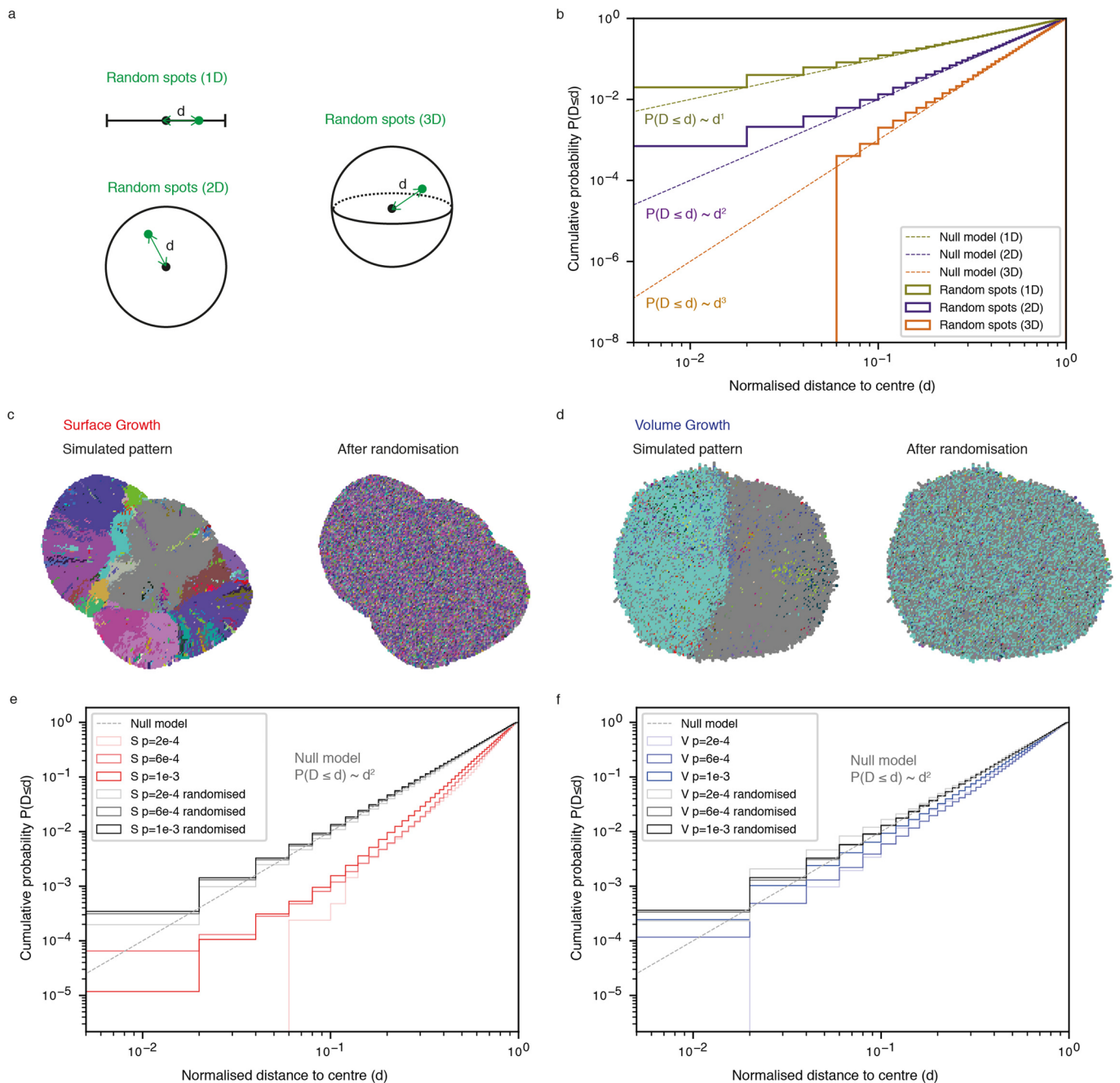
Extended Data Fig. 3 | See next page for caption.

**Extended Data Fig. 3 | Flow diagram illustrating the modules and procedure of simulation.** . Each simulation starts from a single tumour voxel that harbours a *VHL* mutation and 3p loss and runs until the tumour grows to at least 1 million voxels. During a model iteration, events including death, proliferation, acquisition of drivers, and necrosis are evaluated and simulated.

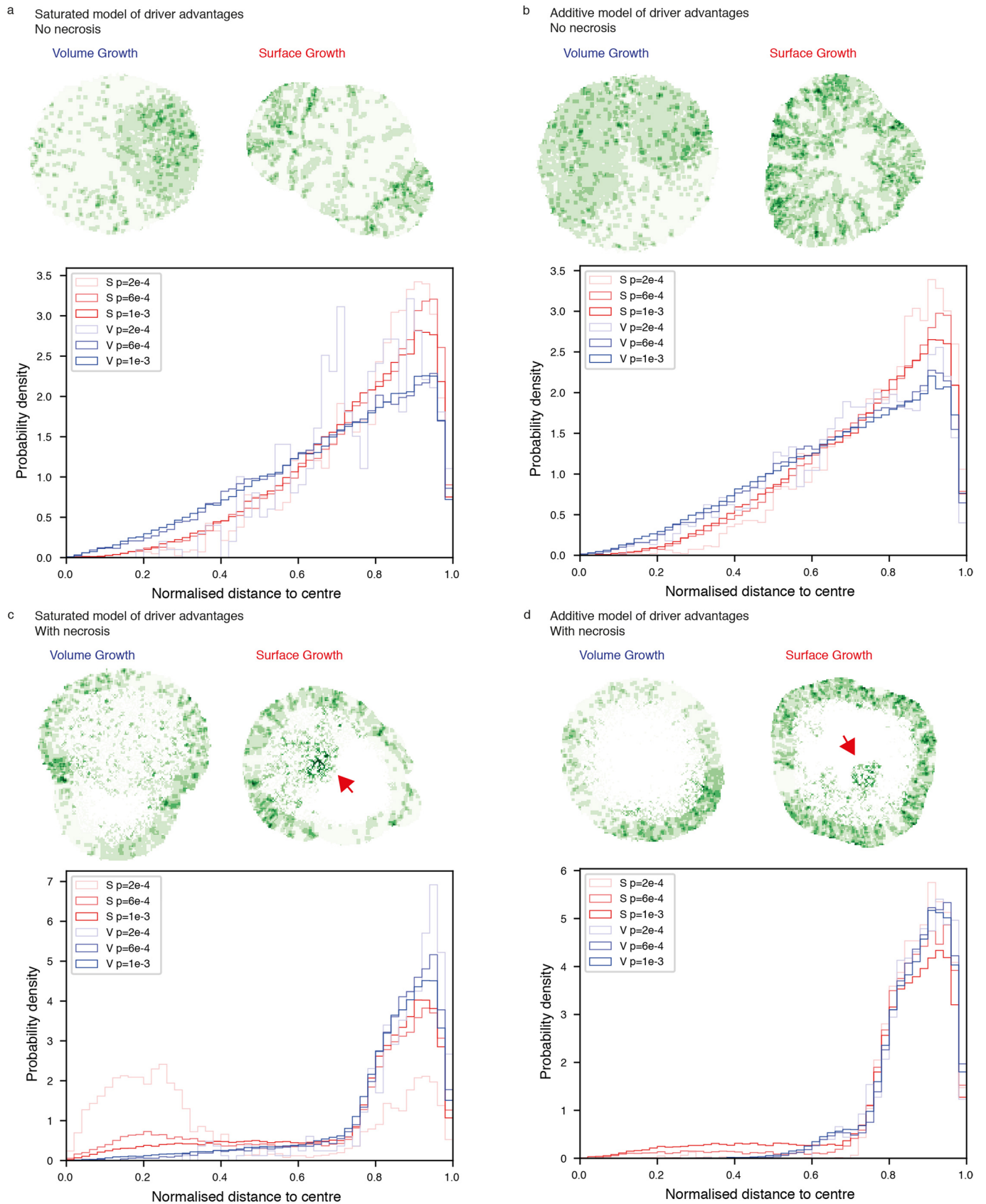




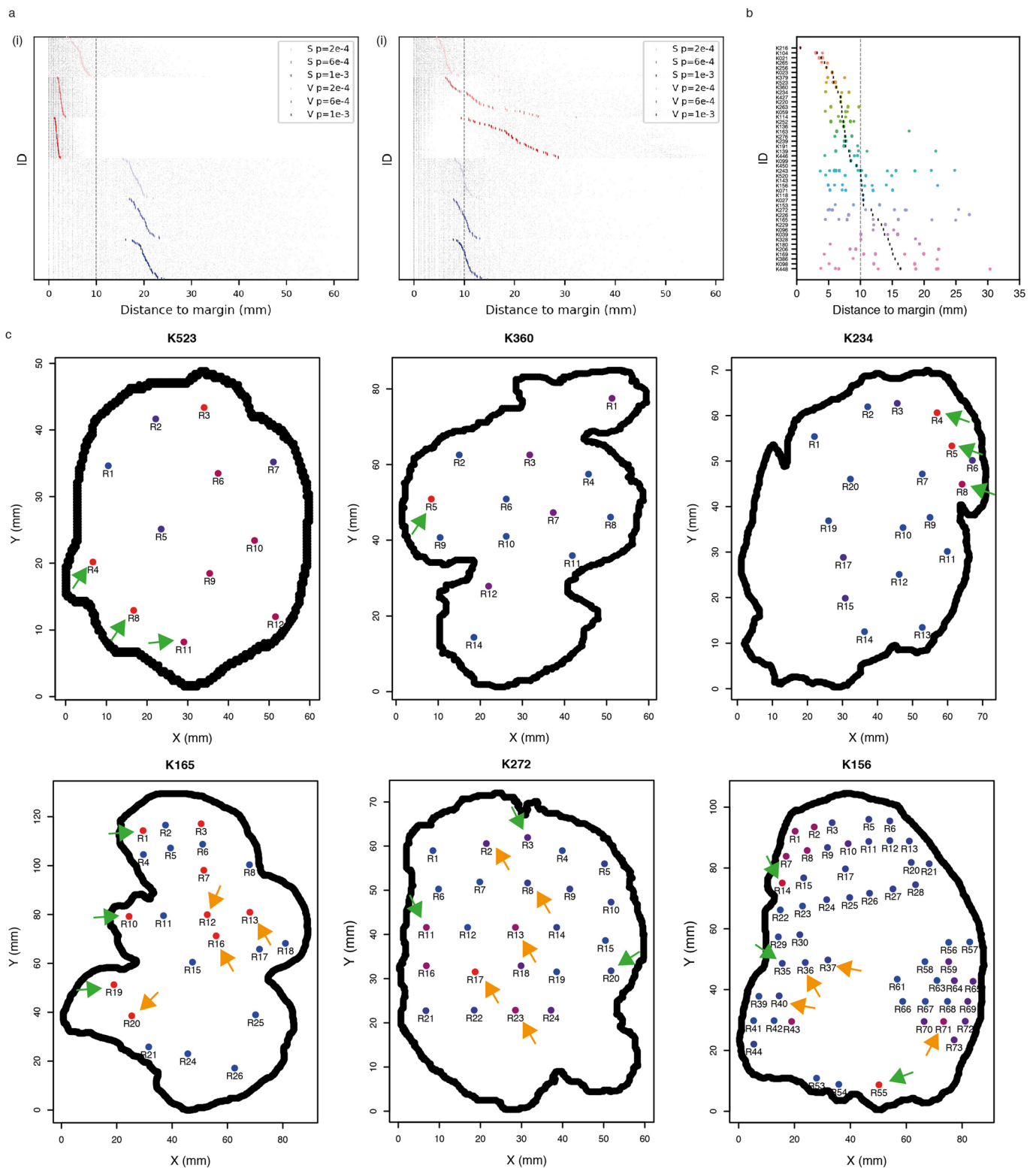
**Extended Data Fig. 4 | Clonal diversity in models with necrosis incorporated.** Whole-tumour CCF of parental clone and largest subclones in *in-silico* tumours under the indicated parameter conditions. Average fitness in a tumour slice for each simulation is presented as a heat map. ‘Parental (3p loss, *VHL*)’ clone is shown along with up to five subclones with a whole-tumour CCF of 0.01 or higher. All remaining subclones are represented in the ‘other’ group.



**Extended Data Fig. 5 | Spatial features of microdiversity in random sampling models and under spatial homogenisation of subclone patterns.** (a) Schematic figure of random sampling of spots in one dimension (1D), two dimensions (2D), and three dimensions (3D). (b) Cumulative probability distribution,  $P(D \leq d)$ , of the normalised distance to tumour centre in null models with spots randomly sampled in 1D (olive), 2D (purple), and 3D (orange). (c-d) Representative examples of a simulated tumour slide before and after spatial homogenisation of subclone patterns in Surface Growth (c) and Volume Growth (d) models, respectively. (e-f) Cumulative probability distribution,  $P(D \leq d)$ , of the normalised distance to tumour centre in models before (red in e, blue in f) and after (grey) spatial homogenisation of subclone patterns, in Surface Growth (e) and Volume Growth (f) models, respectively.

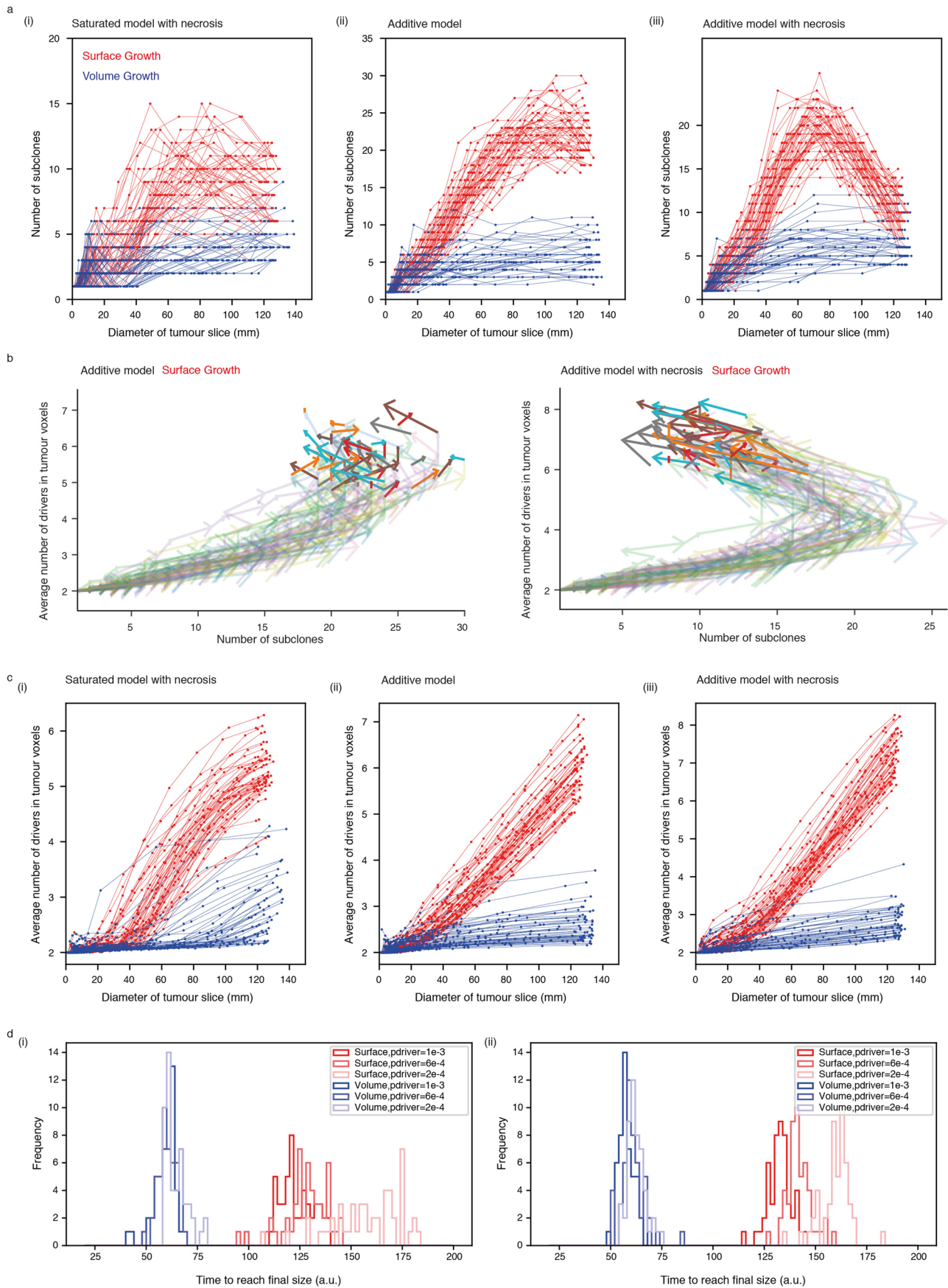


**Extended Data Fig. 6 | Heat maps and spatial features of microdiversity in various model conditions.** (a) Saturated driver advantages without incorporation of necrosis, (b) Additive driver advantages without incorporation of necrosis, (c) Saturated driver advantages with incorporation of necrosis, and (d) Additive driver advantages with incorporation of necrosis.  $N = 50$  simulations for each condition in the probability density distribution plots.



**Extended Data Fig. 7 | The spatial distribution of recent subclones in models with additive driver advantages and in examples of ccRCCs.** (a) Distance from youngest subclones to the tumour margin, in models without (i) or with (ii) incorporation of necrosis.  $N=100$  youngest subclones from each simulation are analysed and shown as grey points, with the mean distance to margin indicated with a coloured vertical bar.  $N=50$  simulations are shown and arranged from small to large mean distance to margin (top to bottom) for each model condition. Surface Growth and Volume Growth models are shown in red and blue, respectively, with increasing driver acquisition probabilities indicated with increasing colour intensity. (b) Distance from regions harbouring events that span a single region to the tumour margin. All tumours that harbour at least one such event are included. The mean distance to margin in a tumour is indicated with a vertical bar. (c) Maps of regional biopsies with the number of subclones within a biopsy colour coded in six cases in the TRACERx Renal study. Two cases (K523 and K156) are also presented in Main Fig. 4. Hues from red to purple to blue reflect decreasing number of subclones. Regions harbouring events that span a single region are marked by arrows: in green if located within 10 mm from the tumour edge and otherwise in orange.

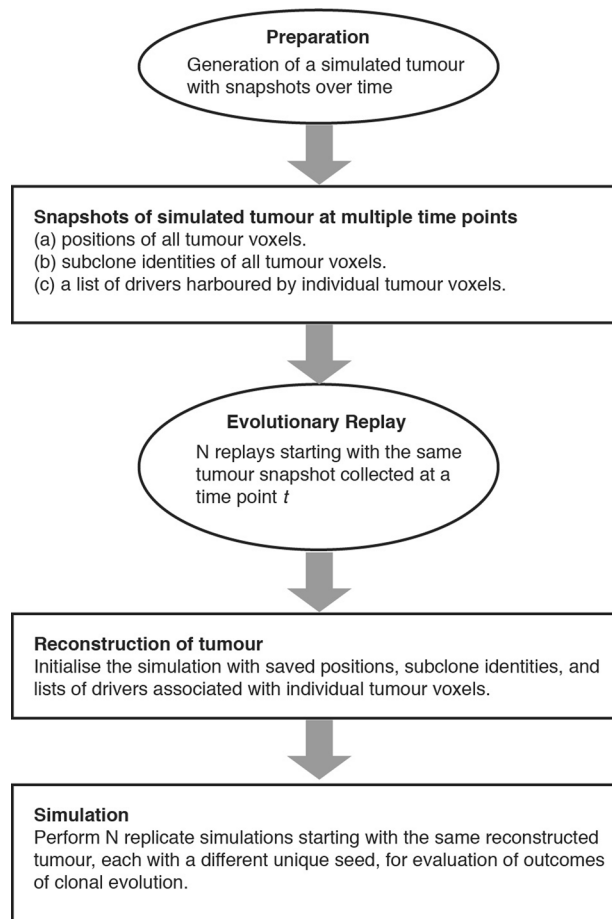




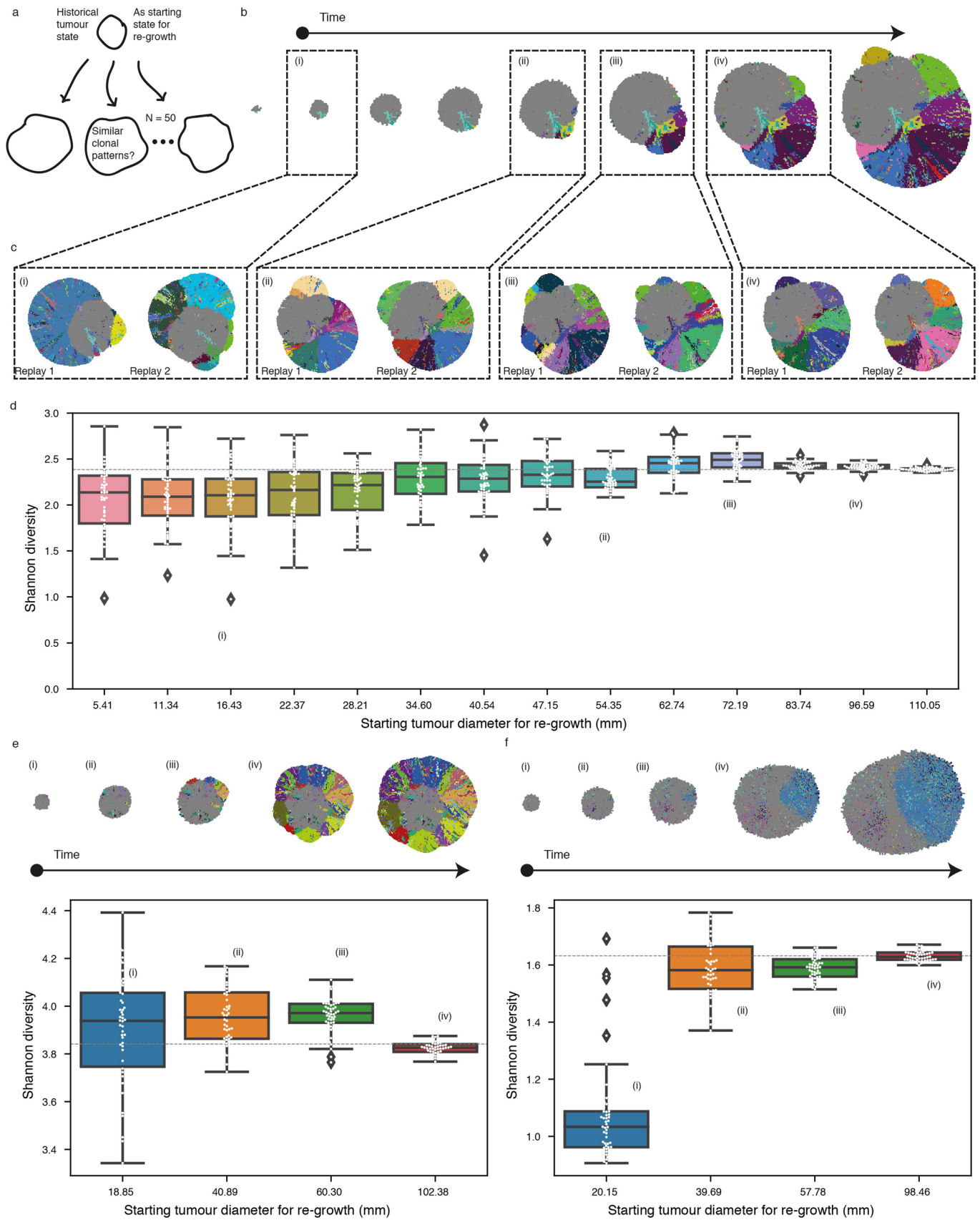
Extended Data Fig. 8 | See next page for caption.



**Extended Data Fig. 8 | Time-course analysis of clonal diversification in various model conditions.** (a) The number of subclones in tumour slice over time in several model conditions: (i) models with saturated driver advantages and necrosis incorporated, (ii) models with additive driver advantages, and (iii) models with additive driver advantages and necrosis incorporated. (b) Vector maps of evolutionary flows over time with respect to the number of subclones and the average number of drivers accumulated among tumour voxels in Surface Growth models without (i) or with (ii) the implementation of necrosis. Models with additive driver advantages are shown. (c) The average number of drivers accumulated in tumour voxels within a tumour slice over time in several model conditions: (i) models with saturated driver advantages and necrosis incorporated, (ii) models with additive driver advantages, and (iii) models with additive driver advantages and necrosis incorporated. (d) The time to reach the final size in Saturated (i) and Additive (ii) models of driver advantages. Volume and Surface Growth models are shown in blue and in red, respectively. In each panel in (a-c),  $N = 50$  simulations with  $p_{driver} = 6 \times 10^{-4}$  are shown.



**Extended Data Fig. 9** | Flow diagram illustrating the procedure of evolutionary replay *in silico*.



Extended Data Fig. 10 | See next page for caption.

**Extended Data Fig. 10 | Evolutionary replay *in silico*.** (a) Schematic figure for description of evolutionary replay. (b) Spatial maps of subclones over time in a representative *in-silico* tumour under Surface Growth with  $p_{driver} = 2 \times 10^{-4}$ . (i)-(iv) mark historical tumour states selected as starting points for evolutionary replay. (c) Spatial maps of subclones at the end of two evolutionary replays that use (i)-(iv) in (b) as starting states. (d) Shannon diversity index at the end of evolutionary replays that start with different historical tumour states. From left to right reflect increasing sizes at which historical tumour states were collected for evolutionary replay. (e-f) Evolutionary replay performed based on *in-silico* tumours under Surface Growth (e) and under Volume Growth with  $p_{driver} = 6 \times 10^{-4}$ , respectively. Dashed line in grey in panels (d-f) reflects the reference Shannon diversity index at the end of the original simulation.

## Reporting Summary

Nature Portfolio wishes to improve the reproducibility of the work that we publish. This form provides structure for consistency and transparency in reporting. For further information on Nature Portfolio policies, see our [Editorial Policies](#) and the [Editorial Policy Checklist](#).

### Statistics

For all statistical analyses, confirm that the following items are present in the figure legend, table legend, main text, or Methods section.

n/a Confirmed

- The exact sample size ( $n$ ) for each experimental group/condition, given as a discrete number and unit of measurement
- A statement on whether measurements were taken from distinct samples or whether the same sample was measured repeatedly
- The statistical test(s) used AND whether they are one- or two-sided  
*Only common tests should be described solely by name; describe more complex techniques in the Methods section.*
- A description of all covariates tested
- A description of any assumptions or corrections, such as tests of normality and adjustment for multiple comparisons
- A full description of the statistical parameters including central tendency (e.g. means) or other basic estimates (e.g. regression coefficient) AND variation (e.g. standard deviation) or associated estimates of uncertainty (e.g. confidence intervals)
- For null hypothesis testing, the test statistic (e.g.  $F$ ,  $t$ ,  $r$ ) with confidence intervals, effect sizes, degrees of freedom and  $P$  value noted  
*Give  $P$  values as exact values whenever suitable.*
- For Bayesian analysis, information on the choice of priors and Markov chain Monte Carlo settings
- For hierarchical and complex designs, identification of the appropriate level for tests and full reporting of outcomes
- Estimates of effect sizes (e.g. Cohen's  $d$ , Pearson's  $r$ ), indicating how they were calculated

*Our web collection on [statistics for biologists](#) contains articles on many of the points above.*

### Software and code

Policy information about [availability of computer code](#)

Data collection

The code for simulation was written in CUDA C++, where Cmake (version 3.12.1) and Cuda compilation tools (release 9.2) were used. This code is used to generate simulated data. Contrast-enhanced CT images were obtained using standard-of-care imaging sequences in 91 patients and curated using a local research PACS (based on the XNAT platform, (Marcus, et al., 2007)).

Data analysis

WebPlotDigitizer (version 4.3) was used to extract X- and Y-coordinates of the macroscopic photos. R (version 3.6.2) was used for generating tumour maps and statistical tests and plotting. Python (version 3.7) and R (version 3.6.2) were used for analysis of simulations. Adobe Illustrator (version 25.1) was used for combining the figure panels. Digital images of Ki67 immunohistochemical staining were analyzed using StrataQuest version 5 (TissueGnostics, Vienna, Austria) for Ki67 quantification.

For manuscripts utilizing custom algorithms or software that are central to the research but not yet described in published literature, software must be made available to editors and reviewers. We strongly encourage code deposition in a community repository (e.g. GitHub). See the Nature Portfolio [guidelines for submitting code & software](#) for further information.

### Data

Policy information about [availability of data](#)

All manuscripts must include a [data availability statement](#). This statement should provide the following information, where applicable:

- Accession codes, unique identifiers, or web links for publicly available datasets
- A description of any restrictions on data availability
- For clinical datasets or third party data, please ensure that the statement adheres to our [policy](#)

Sequencing data that supports this study have been deposited at the European Genome-phenome Archive (EGA), which is hosted by the European Bioinformatics Institute (EBI); accession number EGAS00001002793. Source Data and analysis for generating plots are available in a github repository.



## Field-specific reporting

Please select the one below that is the best fit for your research. If you are not sure, read the appropriate sections before making your selection.

Life sciences       Behavioural & social sciences       Ecological, evolutionary & environmental sciences

For a reference copy of the document with all sections, see [nature.com/documents/nr-reporting-summary-flat.pdf](https://www.nature.com/documents/nr-reporting-summary-flat.pdf)

## Life sciences study design

All studies must disclose on these points even when the disclosure is negative.

Sample size	Estimated enrollment of TRACERx renal trial (NCT03226886): 360. Images were taken for the first 100 patients to match up previously published data.
Data exclusions	Of the 102 macroscopic photos taken, cases in which the whole tumour couldn't be imaged to high quality (n = 9), without a clearly defined boundary between tumour and normal tissues (n = 5), or without exact positions of the biopsy regions (n = 9) were excluded. In total, 79 tumour sections of 66 unique primary tumours were included in this study.
Replication	NA
Randomization	NA; observational study.
Blinding	NA; observational study.

## Reporting for specific materials, systems and methods

We require information from authors about some types of materials, experimental systems and methods used in many studies. Here, indicate whether each material, system or method listed is relevant to your study. If you are not sure if a list item applies to your research, read the appropriate section before selecting a response.

### Materials & experimental systems

n/a	Involved in the study
<input type="checkbox"/>	<input checked="" type="checkbox"/> Antibodies
<input checked="" type="checkbox"/>	<input type="checkbox"/> Eukaryotic cell lines
<input checked="" type="checkbox"/>	<input type="checkbox"/> Palaeontology and archaeology
<input checked="" type="checkbox"/>	<input type="checkbox"/> Animals and other organisms
<input type="checkbox"/>	<input checked="" type="checkbox"/> Human research participants
<input type="checkbox"/>	<input checked="" type="checkbox"/> Clinical data
<input checked="" type="checkbox"/>	<input type="checkbox"/> Dual use research of concern

### Methods

n/a	Involved in the study
<input checked="" type="checkbox"/>	<input type="checkbox"/> ChIP-seq
<input checked="" type="checkbox"/>	<input type="checkbox"/> Flow cytometry
<input checked="" type="checkbox"/>	<input type="checkbox"/> MRI-based neuroimaging

## Antibodies

Antibodies used	Primary antibody used for immunohistochemical staining for Ki67 was rabbit anti-Ki67 (AB16667, Abcam, Cambridge, UK) and secondary antibody was Discovery Omnimap anti-rabbit HRP RUO (760-4311, Roche, Rotkreuz, Switzerland). DAB kit was Discovery Chromomap DAB RUO (760-4311, Roche).
Validation	Validation of rabbit anti-Ki67 (AB16667, Abcam, Cambridge, UK): knockout validation. Reference: Sobecki M, Mrouj K, Camasses A, Parisis N, Nicolas E, Liñares D, et al. The cell proliferation antigen Ki-67 organises heterochromatin. <i>elife</i> . 2016;5:e13722.

## Human research participants

Policy information about [studies involving human research participants](#)

Population characteristics	Of the 101 TRACERx renal clear-cell renal cell carcinoma cases, there were 68 males and 33 females, with the median age of 64 (range: 34 - 84).
Recruitment	TRACERx Renal Inclusion Criteria: 1) Age 18- years or older 2) Patients with histopathologically confirmed renal cell carcinoma, or suspected renal cell carcinoma, proceeding to neoadjuvant therapy and/or nephrectomy/metastasectomy, or identified as having progressive disease 3) Or in patients undergoing nephrectomy for non-malignant disease 4) Medical and/or surgical management in accordance with national and/or local guidelines

5) Written informed consent

Exclusion Criteria:

- 1) Any concomitant medical or psychiatric problems which, in the opinion of the investigator, would prevent completion of treatment or follow-up
- 2) Lack of adequate tissue

Ethics oversight

Royal Marsden NHS Foundation Trust

Note that full information on the approval of the study protocol must also be provided in the manuscript.

## Clinical data

Policy information about [clinical studies](#)

All manuscripts should comply with the ICMJE [guidelines for publication of clinical research](#) and a completed [CONSORT checklist](#) must be included with all submissions.

Clinical trial registration

NCT03226886

Study protocol

Details of the TRACERx Renal clinical study can be found here: <https://clinicaltrials.gov/ct2/show/study/NCT03226886>.

Data collection

Clinical, genomic and follow-up data will be collected between July 6, 2017 and September 1, 2023 (final data collection date for primary outcome measure).

Outcomes

Primary Endpoint: to validate ITH index and WGII as stage and grade independent prognostic markers of progression free survival in patients with ccRCC mutation in a gene of interest.